

Stellar atmospheric parameters of FGK-type stars from high-resolution optical and near-infrared CARMENES spectra

E. Marfil¹,¹★ H. M. Tabernero,^{2,3} D. Montes¹,¹ J. A. Caballero,² M. G. Soto,⁴
J. I. González Hernández,^{5,6} A. Kaminski,⁷ E. Nagel,⁸ S. V. Jeffers,⁹ A. Reiners,⁹
I. Ribas,^{10,11} A. Quirrenbach⁷ and P. J. Amado¹²

¹Facultad de Ciencias Físicas, Departamento de Física de la Tierra y Astrofísica & IPARCOS-UCM (Instituto de Física de Partículas y del Cosmos de la UCM), Universidad Complutense de Madrid, E-28040 Madrid, Spain

²Centro de Astrobiología (CSIC-INTA), ESAC, Camino Bajo del Castillo s/n, E-28691 Villanueva de la Cañada, Madrid, Spain

³Instituto de Astrofísica e Ciências do Espaço, Universidade do Porto, CAUP, Rua das Estrelas, P-4150-762 Porto, Portugal

⁴School of Physics and Astronomy, Queen Mary, University of London, 327 Mile End Rd., E1 4NS London, UK

⁵Departamento de Astrofísica, Universidad de La Laguna, E-38206 La Laguna, Tenerife, Spain

⁶Instituto de Astrofísica de Canarias, vía Láctea s/n, E-38205 La Laguna, Tenerife, Spain

⁷Landessternwarte, Zentrum für Astronomie der Universität Heidelberg, Königstuhl 12, D-69117 Heidelberg, Germany

⁸Hamburger Sternwarte, Gojenbergsweg 112, D-21029 Hamburg, Germany

⁹Institut für Astrophysik, Georg-August-Universität-Göttingen, Friedrich-Hund-Platz 1, D-37077 Göttingen, Germany

¹⁰Institut de Ciències de l'Espai (CSIC), Campus UAB, C/ de Can Magrans s/n, E-08193 Cerdanyola del Vallès, Spain

¹¹Institut d'Estudis Espacials de Catalunya (IEEC), C/ Gran Capità 2-4, E-08034 Barcelona, Spain

¹²Instituto de Astrofísica de Andalucía (IAA-CSIC), Glorieta de la Astronomía s/n, E-18008 Granada, Spain

Accepted 2019 December 28. Received 2019 December 9; in original form 2019 October 4

ABSTRACT

With the purpose of assessing classic spectroscopic methods on high-resolution and high signal-to-noise ratio spectra in the near-infrared wavelength region, we selected a sample of 65 F-, G-, and K-type stars observed with CARMENES, the new, ultra-stable, double-channel spectrograph at the 3.5 m Calar Alto telescope. We computed their stellar atmospheric parameters (T_{eff} , $\log g$, ξ , and $[\text{Fe}/\text{H}]$) by means of the STEPAR code, a PYTHON implementation of the equivalent width method that employs the 2017 version of the MOOG code and a grid of MARCS model atmospheres. We compiled four Fe I and Fe II line lists suited to metal-rich dwarfs, metal-poor dwarfs, metal-rich giants, and metal-poor giants that cover the wavelength range from 5300 to 17 100 Å, thus substantially increasing the number of identified Fe I and Fe II lines up to 653 and 23, respectively. We examined the impact of the near-infrared Fe I and Fe II lines upon our parameter determinations after an exhaustive literature search, placing special emphasis on the 14 *Gaia* benchmark stars contained in our sample. Even though our parameter determinations remain in good agreement with the literature values, the increase in the number of Fe I and Fe II lines when the near-infrared region is taken into account reveals a deeper T_{eff} scale that might stem from a higher sensitivity of the near-infrared lines to T_{eff} .

Key words: line: identification – techniques: spectroscopic – stars: fundamental parameters – stars: solar-type – infrared: stars.

1 INTRODUCTION

The homogeneous, automated computation of stellar atmospheric parameters from stellar spectra, i.e. effective temperature T_{eff} , surface gravity $\log g$, stellar metallicity $[\text{M}/\text{H}]$, and micro-turbulent velocity ξ , plays a crucial role in many astrophysical contexts. First, it leads to the analysis of the fundamental properties of individual

objects as well as of large stellar samples (Valenti & Fischer 2005; Adibekyan et al. 2014). In this regard, large stellar spectroscopic surveys such as RAVE (Steinmetz et al. 2006), APOGEE (Allende Prieto et al. 2008), the *Gaia*-ESO Survey (Gilmore et al. 2012), and GALAH (De Silva et al. 2015) have laid the foundations for our current understanding of the structure and evolution of the Milky Way. Secondly, exoplanetary studies also rely on stellar parameter determinations not only to enable the determination of both planetary radii and masses (e.g. Mann et al. 2019; Schweitzer et al. 2019) but also to characterize the habitable zones around

★ E-mail: emigom01@ucm.es

planet-harboring stars (Kasting, Whitmire & Reynolds 1993; Kopparapu et al. 2013). Furthermore, correlations between the stellar metallicity and planet occurrence rates are now well established and shed light on planet formation mechanisms (Adibekyan et al. 2014; Delgado Mena et al. 2018; Montes et al. 2018).

The equivalent width (EW) method (see e.g. Sousa et al. 2008; Tabernero, Montes & González Hernández 2012; Mucciarelli et al. 2013; Tsantaki et al. 2013; Bensby, Feltzing & Oey 2014; Andreasen et al. 2016) is, along with the spectral synthesis method (see e.g. Valenti & Fischer 2005; Piskunov & Valenti 2017), one of the most widely used spectroscopic techniques for determining stellar atmospheric parameters. A full account of the key caveats of these two methods can be found in Jofré, Heiter & Soubiran (2019) and Blanco-Cuaresma (2019). The advent of high-resolution near-infrared (NIR) spectrographs such as CARMENES (Quirrenbach et al. 2018), SPIRou (Artigau et al. 2014), GIANO (Origlia et al. 2014; Oliva et al. 2018), CRIRES+ (Hatzes & CRIRES + Team 2017), IRD (Kotani et al. 2014), HPF (Wright et al. 2018), and NIRPS (Wildi et al. 2017) allows us to revisit these techniques, originally applied in the optical, in order to assess the impact of the NIR wavelength range on stellar parameter computations. In this context, new observations of FGK-type stars carried out with CARMENES,¹ the double-channel spectrograph at the 3.5 m Calar Alto telescope open up a unique opportunity to test the reliability of such techniques on high-resolution and high signal-to-noise (S/N) ratio spectra in the optical and near-infrared windows.

In this work, we compute the spectroscopic parameters of 65 FGK-type stars selected from a CARMENES stellar library by means of the EW method, which relies on the strength (i.e. the EW measurements) of Fe I and Fe II absorption lines to derive the stellar atmospheric parameters T_{eff} , $\log g$, $[\text{Fe}/\text{H}]$, and ξ assuming local thermodynamic equilibrium. To do so, we followed the approach of Sousa et al. (2007) to automatically measure the EW of the iron lines, and the STEPAP code (Tabernero et al. 2019) to automatically compute the stellar atmospheric parameters imposing excitation and ionization equilibrium conditions on the Fe I and Fe II lines.

The wavelength coverage provided by CARMENES, from 5200 up to 17 100 Å, allowed us to substantially increase the number of Fe I and Fe II lines subject to analysis with the EW method with respect to previous studies restricted to the optical window (Meléndez & Barbuy 2009; Jofré et al. 2014). Furthermore, the high spectral resolution of CARMENES, which is $R = 94\,600$ in the VIS channel and $R = 80\,400$ in the NIR channel (Quirrenbach et al. 2018), significantly improves both the line identification process and the EW measurements. Despite the availability of iron line lists optimized for the NIR region in the literature, the impact on stellar parameter determinations of FGK-type stars is still unknown, mostly due to the fact that such line lists have not as yet been systematically applied to significantly large samples covering a wide portion of the stellar parameter space. For instance, Andreasen et al. (2016) compiled a line list of Fe I and Fe II lines in the region 10 000–25 000 Å, but only tested it against the spectra of the Sun and the F8 IV star HD 20010.

Several other spectral libraries of high-resolution spectra in the near-infrared have been developed over the past few years. For example, Lebzelter et al. (2012) presented the CRIRES-POP spectral library, which provides high-resolution ($R \sim 100\,000$) spectra for 25 stars between B and M spectral types at 1–5 μm . Furthermore, Nicholls et al. (2017) described the data reduction

process and presented the first CRIRES-POP spectral atlas of the K giant 10 Leo. Although the resolution of the spectra in this library is comparable to that of CARMENES, the number of available spectra is significantly lower than the size of the library analysed in this work, and does not satisfactorily cover the parameter space of FGK-type stars. Another example is the IGRINS spectral library (Park et al. 2018), which contains spectra of 84 stars between O and M spectral types in the H (1.49–1.80 μm) and K (1.96–2.46 μm) bands with a resolution of $R = 45\,000$, which is almost half of that provided by CARMENES in the NIR channel. Finally, large surveys such as APOGEE (Zamora et al. 2015; Majewski et al. 2017) have obtained intermediate-resolution ($R \sim 22\,500$) spectra for hundreds of thousands of stars, but with a narrow wavelength coverage in the H band (1.5–1.7 μm).

The analysis performed in this work is structured as follows. In Section 2, we describe the selection of the sample. In Section 3, we outline the main steps of our analysis, including the line selection process and the workflow of the STEPAP code. In Sections 4 and 5, we discuss the results and highlight the conclusions, respectively.

2 SAMPLE

We observed an extensive sample of dwarf, giant, and supergiant stars and brown dwarfs with spectral types from O4 to late L as part of the first open time proposal that used CARMENES. While further details on this stellar library will be provided in forthcoming publications (Caballero et al. in preparation), we start here its scientific exploitation.

From the stellar library we selected 65 stars with spectral types later than F5 and earlier than K4, and projected equatorial rotational velocities $v \sin i < 15 \text{ km s}^{-1}$ (see Table A1). The restriction in spectral type stems from the general limitations of the EW method and hence, STEPAP, as explained in Tabernero et al. (2019), while stars with high rotational velocities have line profiles that cannot be properly fitted by a Gaussian shape, leading to less reliable EW measurements. None of the observed 65 FGK-type stars had a known visual (physical) or optical (non-physical) companion at less than 5 arcsec. However, we excluded from this analysis one of the giants found in the library, c Gem, with spectral type K4.5 III (Keenan & McNeil 1989), as it appeared as an SB2 binary system after cross-correlating its spectrum with the atlas spectrum of Arcturus, as explained in Section 3.1.

Our target list contains 14 *Gaia* benchmark stars (Jofré et al. 2014, 2018; Heiter et al. 2015), including the Sun. The spectrum of the Sun was obtained through the observation of the asteroid 1 Ceres due to the allocation of Calar Alto Director’s discretionary time. According to their original purpose, the fact that the fundamental parameters of these stars have been computed independently from spectroscopy makes them suitable as a reference to assess any method aimed at the automated analysis of cool stars.

Table A1 displays the star names, Henry-Draper numbers, equatorial coordinates from 2MASS (Skrutskie et al. 2006), parallaxes from the *Gaia* Data Release 2 (Gaia Collaboration 2018) if available, and the *Hipparcos* mission (van Leeuwen 2007), along with the spectral types, the values of T_{eff} , $\log g$, ξ , $[\text{Fe}/\text{H}]$ and the stellar projected rotational velocities, $v \sin i$, found in the literature for the selected sample. For the *Gaia* benchmark stars, we adopted the parameters from Jofré et al. (2014) and Heiter et al. (2015), with updated values from Jofré et al. (2018). For the remaining stars, we tabulate the stellar parameters from the most recent references found in the PASTEL catalogue (Soubiran et al. 2016).

¹<http://carmenes.caha.es>

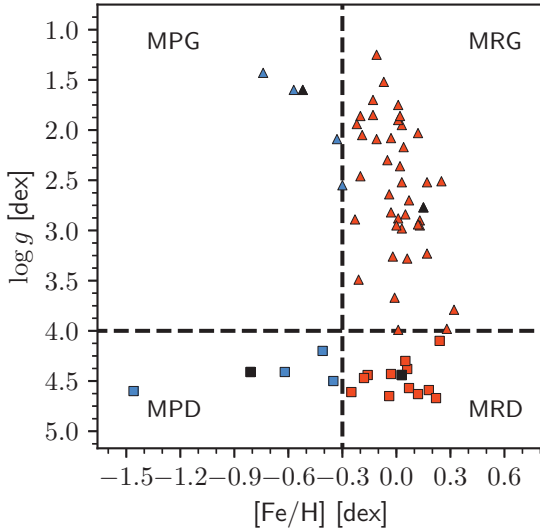


Figure 1. Division of the parameter space in the sample according to the stellar atmospheric parameters found in the literature. The vertical and horizontal dashed black lines represent the boundaries at $[\text{Fe}/\text{H}] = -0.3$ dex and $\log g = 4.0$ dex, respectively, for metal-rich dwarfs (MRDs, orange squares), metal-poor dwarfs (MPDs, blue squares), metal-rich giants (MRGs, orange triangles), and metal-poor giants (MPGs, blue triangles). The stars taken as a reference for each of these regions are shown in black.

Following Tabernero et al. (2019), we divided the parameter space into four different regions in terms of $\log g$ and $[\text{M}/\text{H}]$, using $[\text{Fe}/\text{H}]$ as a proxy of stellar metallicity, in order to simplify our search for iron lines in the CARMENES spectra, as explained in Section 3.2. We thus made a distinction between the dwarf regime, $\log g \geq 4.00$, and the giant regime, $\log g < 4.00$, and between metal-rich stars, $[\text{Fe}/\text{H}] > -0.30$, and metal-poor stars, $[\text{Fe}/\text{H}] \leq -0.30$. We dubbed the four resulting line lists metal-rich dwarfs (MRDs), metal-poor dwarfs (MPDs), metal-rich giants (MRGs), and metal-poor giants (MPGs). We selected the following *Gaia* benchmark stars, all of which were observed with CARMENES, as a reference for the assembly of the corresponding Fe I and Fe II line lists: 18 Sco for the MRD, μ Cas for the MPD, ϵ Vir for the MRG, and Arcturus for the MPG. We show this division of the parameter space in Figs 1 and 2.

3 ANALYSIS

3.1 Data processing

The 65 pairs of VIS and NIR spectra were taken in service mode between 2016 March and 2016 June with the two CARMENES channels operating simultaneously. In general, exposure times were manually adjusted to reach an S/N between 100 and 300 in the *J* band. The observations were carried out without the simultaneous wavelength calibration of the Fabry–Pérot etalons since there was no particular interest in precise radial velocity determinations (i.e. better than ~ 20 m s $^{-1}$) for these stars.

The spectra were taken in ‘target + sky’ mode, i.e. the stars were observed in fibre A and the sky in fibre B. Both fibres are identical but fibre B is located at 88 arcsec to the east. Star and sky spectra are available through the Calar Alto archive. In our work, we did not subtract the corresponding sky spectrum to each star spectrum, as this is an ongoing analysis (Nagel et al. in preparation).

The raw spectra were reduced with the CARACAL pipeline (Zechmeister, Anglada-Escudé & Reiners 2014; Caballero et al.

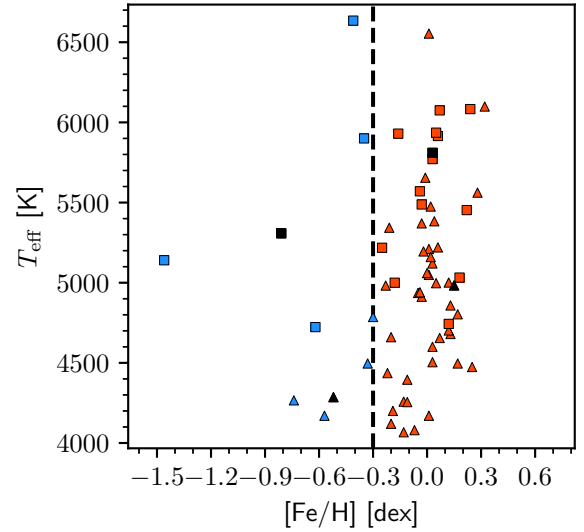


Figure 2. Same as Fig. 1, but for literature values of T_{eff} versus $[\text{Fe}/\text{H}]$ in the sample. Only the boundary at $[\text{Fe}/\text{H}] = -0.3$ dex is shown.

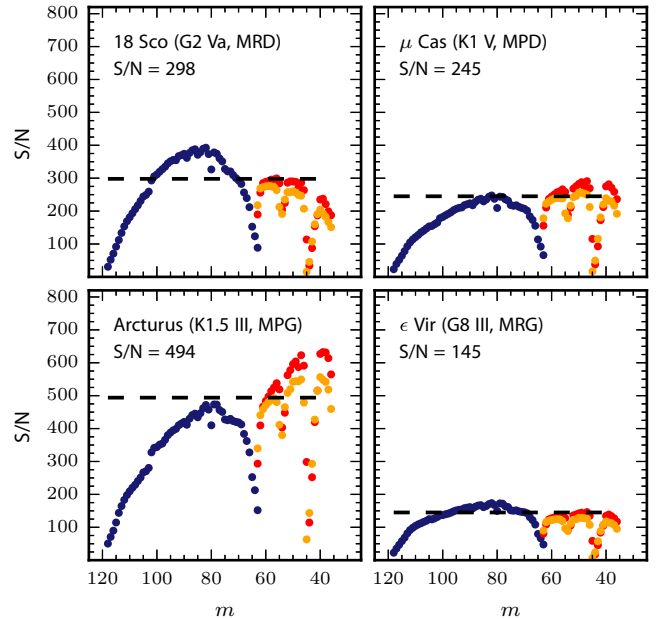


Figure 3. CARACAL S/N of the CARMENES spectra of the reference stars (18 Sco, μ Cas, ϵ Vir, and Arcturus) as a function of the spectral order m . The blue circles are the orders in the VIS channel, while the orange and red circles are the two HgCdTe array detectors of the NIR channel. The dashed black lines mark the global S/N estimation given by iSpec.

2016), which is based on the IDL REDUCE package (Piskunov & Valenti 2002). CARACAL generates one fully reduced, wavelength-calibrated, one-dimensional spectrum of the individual spectral orders. Fig. 3 displays the CARACAL S/N of the four reference spectra as a function of the diffraction order m . We estimated the global S/N of the spectra with the integrated Spectroscopic framework (iSpec, see Blanco-Cuaresma et al. 2014) in terms of the median of the flux values divided by their corresponding flux errors. The global S/N of the selected spectra can also be found in Table A2.

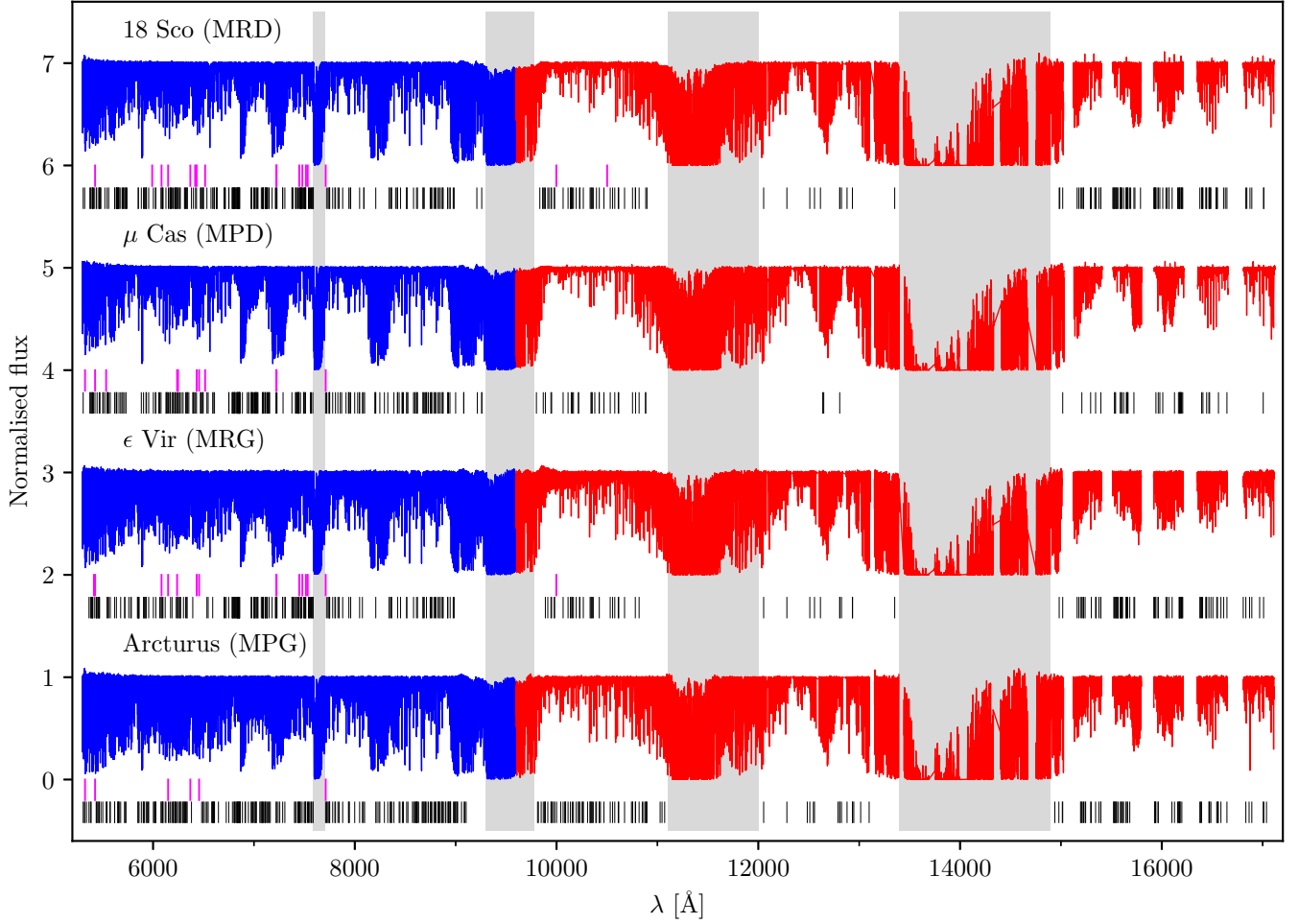


Figure 4. Distribution of the selected Fe I and Fe II absorption lines in the reference spectra. The Fe I and Fe II lines are shown as black and pink vertical lines, respectively, below the spectra. The VIS and NIR channels of the CARMENES instrument are shown in blue and red, respectively. The grey shaded areas show the regions severely affected by telluric absorption.

Next, we employed a wavelength grid to merge the spectral orders of both channels into one single spectrum. The wavelength grid, which is evenly spaced on a logarithmic scale, mirrors the natural wavelength spacing of the CARMENES spectrographs across the orders. In Fig. 4, we show the normalized, merged spectra of the four stars taken as a reference in this work.

Since the CARMENES instrument operates in vacuum, we performed a vacuum-to-air wavelength conversion of the order-merged, channel-merged, CARMENES spectra to provide the wavelengths of the Fe I and Fe II lines on an air scale, following the International Astronomical Union standard (Morton 2000):

$$\lambda_{\text{air}} = \frac{\lambda_{\text{vacuum}}}{n}, \quad (1)$$

where n is the refraction index, which is given by the following expression:

$$n = 1 + 8.34254 \times 10^{-5} + \frac{2.406147 \times 10^{-2}}{130 - s^2} + \frac{1.5998 \times 10^{-4}}{38.9 - s^2}, \quad (2)$$

where $s = 10^4/\lambda_{\text{vacuum}}$, with λ_{vacuum} in Å.

After the vacuum-to-air wavelength conversion, we accounted for the barycentric velocity of the observatory at the time of observations. We then computed the radial velocities with iSpec by means of the cross-correlation function between the observed

CARMENES spectra and a template spectrum provided by iSpec in the following way. In the dwarf regime, we set as the template a solar spectrum based on data from the NARVAL (Aurière 2003) and HARPS (Mayor et al. 2003) instruments (see Blanco-Cuaresma et al. 2014) covering the overlap region with CARMENES, i.e. the 5200–10 480 Å range. Likewise, in the giant regime we set as the template spectrum an atlas of Arcturus covering the 5200–9260 Å range (Hinkle et al. 2000). Both template spectra were corrected from telluric absorption features, which makes them suitable for cross-correlation. This allowed us to correct the spectra from the corresponding Doppler shift. In Fig. 5, we compare the radial velocities thus computed against the literature values. Four stars exhibit a difference in radial velocity greater than 1 km s^{−1} compared to literature values. These are all single-lined (SB1) spectroscopic binaries: μ Cas (Worek & Beardsley 1977), α CMi (Girard et al. 2000), α UMa (Spencer Jones & Furner 1937), and ζ Her (Scarfe et al. 1983). The radial velocities of our sample can also be found in Table A2. The average difference in the computed radial velocities of the sample with respect to the literature values is 0.09 ± 0.64 km s^{−1}.

3.2 Fe I and Fe II line selections

We requested four line lists from the Vienna Atomic Line Database (VALD3; Piskunov et al. 1995; Kupka et al. 2000,

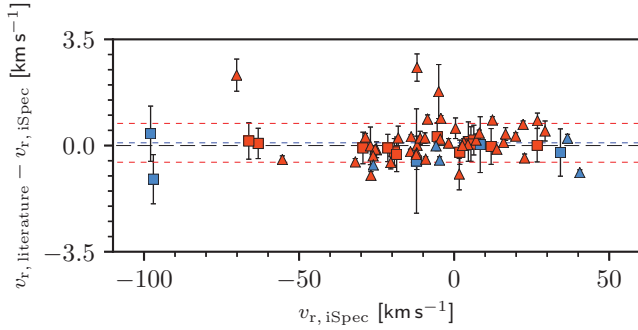


Figure 5. Comparison between the radial velocities v_r of the sample obtained with iSpec and the literature values. Symbols are the same as in Fig. 1. The dotted blue and red lines are the average difference and the corresponding 1σ dispersion, respectively.

1999; Ryabchikova et al. 2015), corresponding each to one of our four reference spectra. We used the option `Extract stellar` available at the VALD3 website,² with a wavelength range from 5300 to 17 100 Å, a minimum line depth of 5 per cent with respect to the continuum flux, and the corresponding input stellar parameters found in Table A1. We excluded the wavelength range 5200–5300 Å from this search because of the low S/N of the CARMENES spectra in this region.

Because of its user-friendly interface, we used iSpec to select the Fe I and Fe II spectral lines by visually projecting the VALD3 line list files on to the corresponding processed reference spectra. We rejected Fe I and Fe II lines that showed spectral blending with close atomic and molecular lines. Since telluric lines are ubiquitous in the near-infrared and at the red end of the optical (see e.g. Reiniers et al. 2018), we computed a synthetic transmission spectrum via the telluric-correction tool `molecfit` (Kausch et al. 2015; Smette et al. 2015), which makes use of the line-by-line radiative transfer model (LBLRTM, Clough et al. 2005) and the HITRAN molecular line data base (Gordon et al. 2017), to model the Earth’s atmospheric transmission spectrum. This allowed us to prevent wrong line identification throughout the visual inspection of the reference spectra. Further details on the telluric correction of the CARMENES spectra can be found in Passegger et al. (2019). A full description of the correction will appear in a forthcoming publication of the CARMENES series (Nagel et al. in preparation).

To expedite our analysis, we also looked for Fe I and Fe II line compilations found in the literature that overlap with the wavelength range covered by CARMENES. Since the careful analysis of the optical wavelength range up to ~ 6860 Å has already led to several line lists published in previous works that were specifically compiled to yield the best possible set of stellar atmospheric parameters for FGK-type stars (see e.g. Sousa et al. 2008; Jofré et al. 2014; Tabernero et al. 2019), we refrained from further refining the line selection in this window and adopted the iron lines given in Sousa et al. (2008). As to the near-infrared region, we checked our iron line selections from 10 000 to 17 100 Å against the ones tabulated in Andreasen et al. (2016). Despite our careful search for Fe II in the NIR region, we only found one Fe II line at $\lambda = 10\,501.503$ Å. Finally, iron lines found in the region 6 800–10 000 Å were not compared with the literature due to the lack of line compilations in this spectral window. In Table 1, we show a summary of the number of iron lines listed in this work on a global and per-line list basis, i.e.

Table 1. Number of Fe I and Fe II lines reported in this work, Sousa et al. (2008, Sou08), Andreasen et al. (2016, And16), and Tabernero et al. (2019, Tab19), from 5300 to 17 100 Å.

Reference	Line list/region	#lines	
		Fe I	Fe II
This work	MRD	386	16
This work	MPD	295	9
This work	MRG	306	13
This work	MPG	379	4
This work	CARMENES VIS channel	437	21
This work	CARMENES NIR channel	216	2
This work	Globally	653	23
Tab19	MRD	112	8
Tab19	MPD	82	8
Tab19	MRG	72	7
Tab19	MPG	95	5
Tab19	Globally	175	14
Sou08	–	172	19
And16	–	272	12

MRD, MPD, MRG, and MPG, in comparison with those tabulated in Sousa et al. (2008) and Andreasen et al. (2016) in the wavelength region covered by CARMENES.

Since we assembled the line lists considering four specific reference spectra, we removed the Fe I and Fe II line identifications that fall into any of the CARMENES inter- and intra-order gaps³ as a consequence of the corresponding Doppler shift corrections in the remaining spectra of the sample.

In Fig. 4, we show the distribution of the selected Fe I and Fe II lines in the reference spectra. In addition, in Fig. A1 we give a close-up view of the spectrum of the reference, solar-type star 18 Sco along with the line selections. We give the central wavelength in air, λ_{air} , the excitation potential, χ , and the oscillator strength, $\log gf$, of the selected Fe I and Fe II lines in Tables A4 and A5, respectively.

3.3 EW measurements

We computed the EWs by fitting Gaussian profiles to the absorption lines,⁴ as shown in Fig. 6. First, we selected a region approximately 6 Å wide centred at the selected absorption line, λ , and performed a continuum normalization on the spectra following Sousa et al. (2007). Specifically, we fitted a third-degree polynomial to the data, selecting only the points that lie within rejt times the polynomial, where $\text{rejt} = 1 - 1/(S/N)$, and S/N is the signal-to-noise ratio of the region. We then identified the absorption lines present in the spectra by finding the points where the first derivative of the data was zero, and the second derivative was positive. Finally, we fitted Gaussian profiles to the lines detected, and integrated the profile corresponding to the selected line λ to obtain the EW. The uncertainty in the EW was estimated by changing the Gaussian parameter estimates within 1σ of their uncertainty for a total of 1000 iterations, and looking at the EW distribution.

As in Tabernero et al. (2019), we only considered lines with $10 \text{ mÅ} < \text{EW} < 120 \text{ mÅ}$ for all stars in the sample to avoid problems with line profiles of very intense lines and potentially bad EW measurements of extremely weak lines.

³<http://carmenes.caha.es/ext/instrument/>

⁴The code is available at: <https://github.com/msotov/EWComputation>

²<http://vald.astro.uu.se>

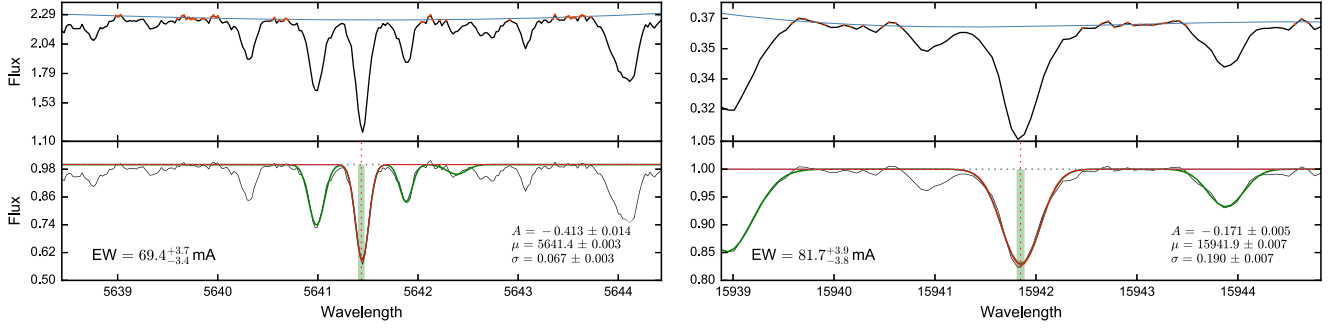


Figure 6. EW measurements of two Fe I lines in the spectrum of 18 Sco, at 5641.434 Å (left) and 12824.859 Å (right). The upper panels illustrate the continuum determination, where the points used for the final polynomial fit are highlighted in red. The bottom panels show the full fit performed for all detected lines, shown in green, and the Gaussian fit of the selected line, shown in red, parametrized by the central intensity in normalized units, A , the central wavelength in Å, μ , and the Gaussian dispersion, σ . The shaded red area depicts the 1σ confidence intervals of the Gaussian fit, and the green square, the EW estimation, as explained in the text.

3.4 STEPAR

The STEPAR code⁵ is a PYTHON implementation of the EW method specifically designed for the automated and simultaneous computation of the stellar atmospheric parameters of FGK-type stars, namely T_{eff} , $\log g$, $[\text{Fe}/\text{H}]$, and ξ . STEPAR is one of the 13 pipelines in the *Gaia*-ESO Survey used in the analysis of UVES U580 spectra of late-type, low-mass stars. A full description of its workflow and performance can be found in Tabernero et al. (2019). STEPAR is an iterative code that derives the stellar parameters and their associated uncertainties by imposing both excitation and ionization equilibrium conditions on a set of Fe I and Fe II lines, using the 2017 version of the MOOG⁶ code (Sneden 1973) and a grid of plane-parallel and spherical MARCS⁷ model atmospheres (Gustafsson et al. 2008).

For any given MOOG-compliant EW input file comprised of a significant number of Fe I and Fe II lines, STEPAR follows a Downhill Simplex minimization algorithm (Press et al. 2002) across the parameter space in order to find the stellar atmospheric parameters that best reproduce the observed EWs. The code takes $T_{\text{eff}} = 5777$ K, $\log g = 4.44$ dex, and $\xi = 1.0$ km s⁻¹ as the initial input values.

If we let $\epsilon(\text{Fe})$ represent the iron abundance retrieved from any given Fe line and χ be the excitation potential of the line, STEPAR iterates until the slopes of χ versus $\log \epsilon(\text{Fe I})$ and $\log \text{EW}/\lambda$ versus $\log \epsilon(\text{Fe I})$ are zero, i.e. the iron atoms are in excitation equilibrium. It also imposes ionization equilibrium so that $\log \epsilon(\text{Fe I}) = \log \epsilon(\text{Fe II})$. Throughout this iterative process, the code verifies that the average $[\text{Fe}/\text{H}]$ in the MOOG output is always compatible with the iron abundance of the input atmospheric model. Next, STEPAR performs an individual σ clipping on the Fe I and Fe II lines to remove the ones that imply an iron abundance, $\log \epsilon(\text{Fe})$, that exceeds the 3σ limit with respect to the median abundance of all lines. After this step, STEPAR restarts the minimization algorithm with the remaining Fe I and Fe II lines, taking as initial input values the parameters computed in the first run. STEPAR computes the uncertainties in the stellar atmospheric parameters following the sequence: $\delta\xi$, δT_{eff} , $\delta \log g$, and $\delta[\text{Fe}/\text{H}]$. This computation relies on the retrieved Fe I and Fe II abundances and the uncertainties in the slopes that define the equilibria conditions. The code also propagates

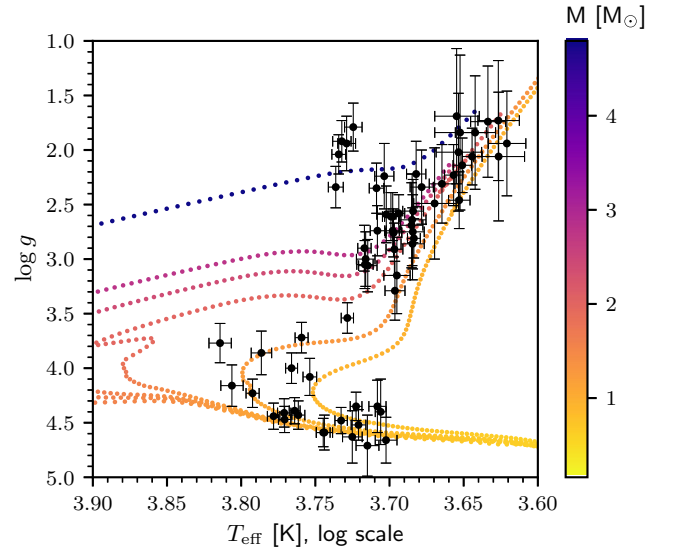


Figure 7. Kiel diagram ($\log g$ versus $\log T_{\text{eff}}$) of the sample along with the YaPSI isochrones at 0.1, 0.4, 0.6, 1, 4, and 13 Ga (for $Z = 0.016$, see Spada et al. 2017).

the uncertainties following the previous sequence. For example, the uncertainty in $[\text{Fe}/\text{H}]$ is a quadrature between the standard deviation of the Fe I and Fe II abundances and the propagated uncertainties in the remaining stellar parameters. Further details on the computation of the uncertainties can be found in Tabernero et al. (2019).

4 RESULTS AND DISCUSSION

In Table A2, we give the stellar atmospheric parameters of the sample computed with STEPAR. These were obtained after matching the corresponding Fe I and Fe II line lists to the stars according to their reference parameters reported in Table A1.

We also performed the analysis of the sample with the EW method taking into account only the Fe I and Fe II lines found in the optical region covered by the VIS channel of the CARMENES instrument. The parameters thus obtained can be found in Table A3. Unfortunately, we could not attempt to analyse the NIR in the same manner because of the scarcity of Fe II lines above 9600 Å.

In Fig. 7, we display a Kiel diagram, i.e. $\log g$ versus $\log T_{\text{eff}}$, of our sample as computed with STEPAR, along with the Yale–Potsdam

⁵STEPAR is available at: <https://github.com/hmtabernero/StePar>

⁶<https://www.as.utexas.edu/~chris/moog.html>

⁷<http://marcs.astro.uu.se>

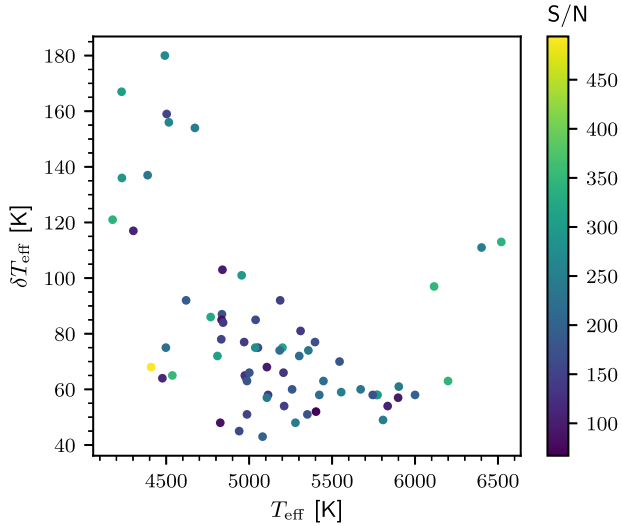


Figure 8. Uncertainties in T_{eff} , δT_{eff} , versus T_{eff} for our sample, as computed with STEPAR.

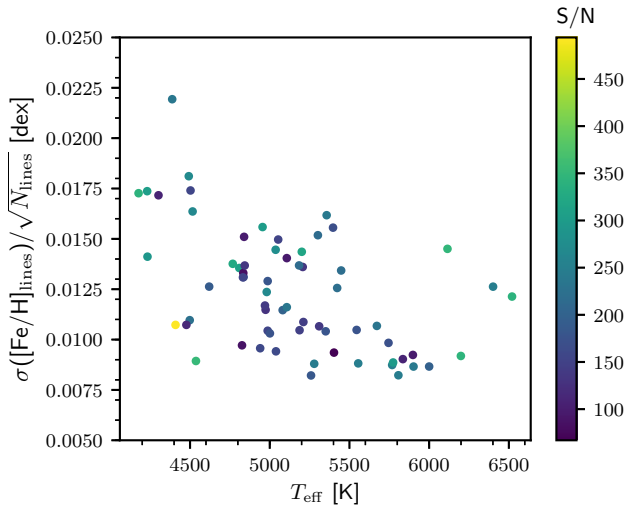


Figure 9. Line-to-line scatter in [Fe/H] versus T_{eff} and S/N in the sample.

Stellar Isochrones (YAPSI, Spada et al. 2017) at solar metallicity, namely $Z = 0.016$. Overall, we found no disparity between our derived values and the region of the parameter space covered by the isochrones. As pointed out by Tabernero et al. (2019), STEPAR returns slightly higher effective temperatures for F-type dwarfs. Five luminous, G-type, giant stars (β Dra, F Hya, ϵ Leo, 37 LMi, and ζ Mon) are located at an anomalous position in the Kiel diagram. According to Luck (2014), these stars are thought to be the evolved counterparts of early F- to B-type main-sequence stars that have reached the He-burning evolutionary stage.

In the cool regime, i.e. K-type stars, where stellar spectra become increasingly more crowded, the continuum placement is more uncertain, and the iron lines are subject to blending with other spectral features. On the other hand, sufficiently strong iron lines become increasingly scarce towards early F-type stars. This has a strong impact on the computed errors in the stellar atmospheric parameters, in particular the effective temperature, and the line-to-line scatter in [Fe/H], as shown in Figs 8 and 9, respectively.

In Figs 10 and 11, we compare the stellar atmospheric parameters computed with STEPAR with values from the literature (McWilliam 1990; Heiter & Luck 2003; Allende Prieto et al. 2004; Valenti & Fischer 2005; Hekker & Meléndez 2007; Liu et al. 2007; Sousa et al. 2008; Takeda, Sato & Murata 2008; Lyubimkov et al. 2010; Wu et al. 2011; Thygesen et al. 2012; Santos et al. 2013; Jofré et al. 2014, 2015; Luck 2014; Morel et al. 2014; da Silva, Milone & Rocha-Pinto 2015; Jofré et al. 2018), taking into account the VIS and NIR channels simultaneously, and only the VIS channel, respectively. To explore possible sources of potential systematic trends or offsets, we followed the Monte Carlo method implemented in Tabernero et al. (2018). We generated 10 000 synthetic samples based on our derived stellar atmospheric parameters. We computed all data points in each of these artificial samples by means of a normal distribution centred at the original measurements, and took the uncertainties in each parameter as the width of the distribution. The summary of the Monte Carlo simulations can be found in Table 2. We computed the Pearson and Spearman correlation coefficients, which quantify the degree of correlation between any two given variables. We found a significant correlation in the differences between our own T_{eff} values and the literature versus the literature values. However, no such correlation was found in the derived $\log g$ and [Fe/H] values.

At first glance, it seems that our temperature scale has an intrinsic systematic error with respect to the literature values. The offset appears to be linked to the fact that we now include the NIR channel, given that the correlation diminishes when we restrict the analysis to the iron lines found in the VIS channel. Although the STEPAR code could be thought to be the underlying reason for this correlation, we are not comparing the same temperature scale. In other words, we now take into account iron absorption lines in a wavelength region that is different from most studies found in the literature. In addition, this offset is more noticeable for the coolest stars. The former result could arise from the fact that the NIR lines are more sensitive to the effective temperature than the optical lines, at least for the cool stars. In other words, although the inclusion of the NIR in the analysis does not bring extreme differences of the derived stellar parameters with respect to the analysis using the optical range, it seems to reveal a deeper T_{eff} scale as suggested by the meaningful correlation found in Table 2 as well as Figs 10 and 11.

In Fig. 12, we show the values of $\log g$ derived with STEPAR against those obtained adopting the distances from *Gaia* DR2 (Gaia Collaboration 2018), if available, and the *Hipparcos* mission (van Leeuwen 2007). We computed the latter $\log g$ values by means of the PARAM web interface⁸ (da Silva et al. 2006; Rodrigues et al. 2014, 2017), which employs a Bayesian approach to derive the stellar parameters, including stellar age, mass, and radius. The $\log g$ values obtained with PARAM can be found in Tables A2 and A3. Following the Monte Carlo method described above, we found a systematic offset of 0.15 ± 0.38 dex. The Pearson and Spearman correlation coefficients, which are $r_p = -0.302 \pm 0.093$ and $r_s = 0.259 \pm 0.104$, respectively, reveal a correlation of around 9 per cent, which is slightly lower than previous works (see e.g. Tabernero et al. 2017).

Regarding the micro-turbulent velocity, Fig. 13 shows the values of ξ obtained with STEPAR against the literature. Our derived values for ξ are compatible with the literature values to a large extent. However, six stars (i.e. β Dra, F Hya, ζ Mon, σ Oph, θ Her, and HD 77912), with computed ξ values larger than 3 km s^{-1} , show larger deviations with respect to the literature, which can be as large

⁸<http://stev.oapd.inaf.it/cgi-bin/param>

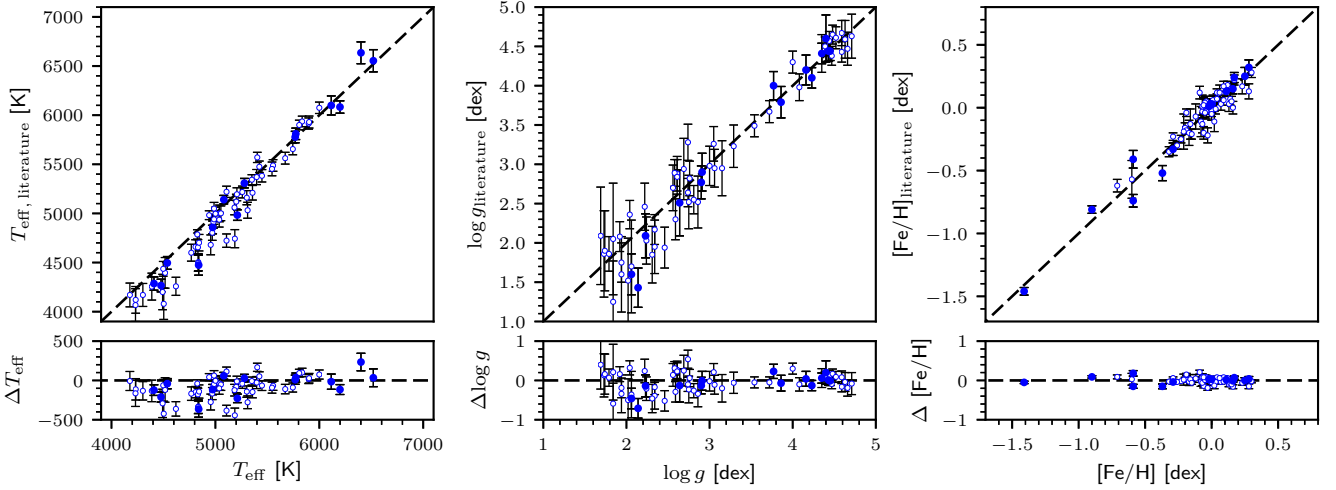


Figure 10. Comparison between the stellar atmospheric parameters obtained with STEPAR including the VIS and NIR channels of CARMENES and the literature values. The blue filled circles are the *Gaia* benchmark stars in our sample. The remaining stars in the sample are shown with the blue open circles. The dashed black lines indicate the one-to-one relationship. From left to right: T_{eff} , $\log g$, and $[\text{Fe}/\text{H}]$.

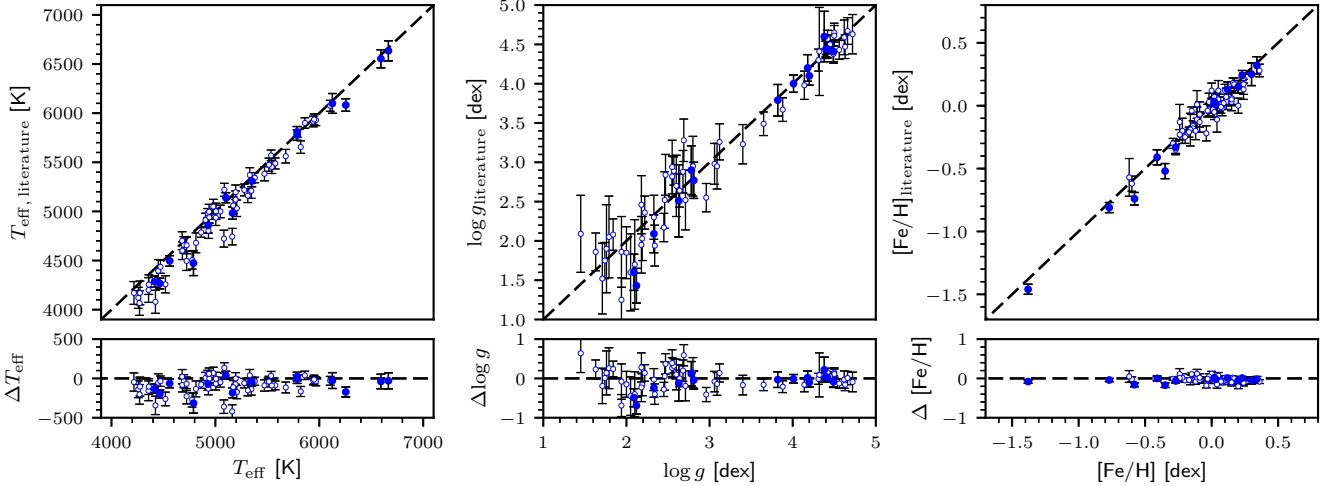


Figure 11. Same as Fig. 10 but restricting the analysis to the FeI and FeII lines found in the optical wavelength region covered by the VIS channel of CARMENES.

Table 2. Summary of the Monte Carlo simulations carried out on the T_{eff} , $\log g$, and $[\text{Fe}/\text{H}]$ values of the sample as computed with STEPAR. We show the average difference on each parameter and the values of the Pearson (r_p) and Spearman (r_s) correlation coefficients.

Parameter	Difference	r_p	r_s
VIS and NIR channels			
T_{eff} [K]	-100 ± 166	0.40 ± 0.07	0.41 ± 0.07
$\log g$ [dex]	-0.03 ± 0.38	0.10 ± 0.10	0.07 ± 0.11
$[\text{Fe}/\text{H}]$ [dex]	0.00 ± 0.11	-0.09 ± 0.06	-0.12 ± 0.07
VIS channel only			
T_{eff} [K]	-92 ± 135	0.21 ± 0.08	0.21 ± 0.09
$\log g$ [dex]	-0.01 ± 0.38	-0.01 ± 0.10	0.00 ± 0.10
$[\text{Fe}/\text{H}]$ [dex]	-0.04 ± 0.10	-0.01 ± 0.08	-0.07 ± 0.09

as 1.6 km s^{-1} , as in the case of the star ζ Mon. In addition, we retrieved a significantly lower ξ value for the star ν Boo compared to the literature. Although ξ and $[\text{Fe}/\text{H}]$ are thought to be partially degenerate (Valenti & Fischer 2005), we fail to identify the impact that such high or low ξ values have on $[\text{Fe}/\text{H}]$ for these stars in our analysis. For example, a difference of 1.6 km s^{-1} in ξ for the star ζ Mon leads to a difference of only 0.07 dex in $[\text{Fe}/\text{H}]$ between the literature and the analysis with STEPAR, and both computed and literature values are compatible within error bars.

A closer look at the comparison between our parameter determinations and the *Gaia* benchmark star parameters from Heiter et al. (2015), with updated values from Jofré et al. (2018), can be found in Fig 14. We find good agreement between our derived values and the fundamental T_{eff} and $\log g$, i.e. derived from the fundamental relations $L = 4\pi R^2 \sigma T_{\text{eff}}^4$ and $g = GM/R^2$, respectively, by means of specific information that is available for these stars, such as the parallax, the angular diameter, and the bolometric flux. None the less, we note four outliers in T_{eff} ($\Delta T_{\text{eff}} > 200 \text{ K}$) and two in $\log g$

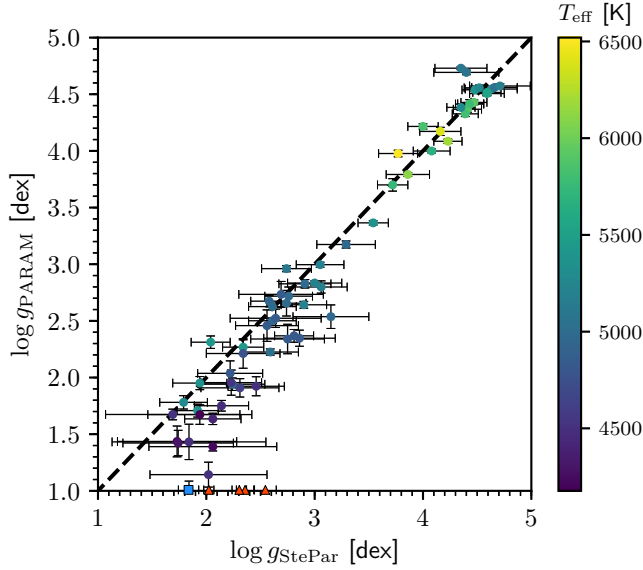


Figure 12. Surface gravities, $\log g$, derived for the sample with STEPAR versus those obtained with the code PARAM, adopting the distances from *Gaia* DR2.

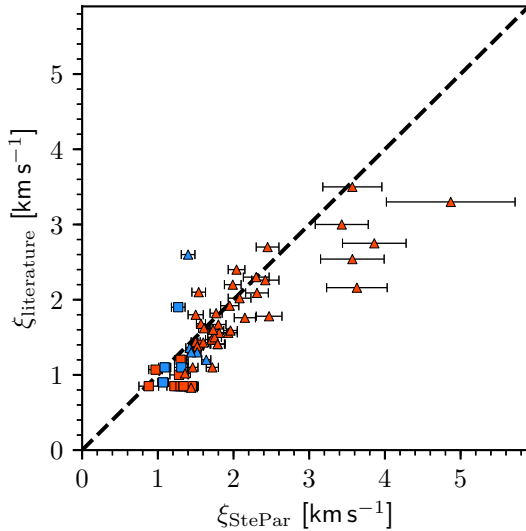


Figure 13. Micro-turbulent velocity derived for the sample with STEPAR, ξ_{StePar} , versus literature values. Symbols are the same as in Fig. 1.

($\Delta \log g > 0.25$ dex). Among the outliers in $\log g$ are Arcturus and 7 Psc. According to Heiter et al. (2015), the $\log g$ value of Arcturus remains uncertain, with literature values ranging from 1.4 up to 2.0 dex, while both the T_{eff} and $\log g$ values for the star 7 Psc are, in fact, not recommended for use as reference values. Among the outliers in T_{eff} are the stars HD 49933, μ Leo, ϵ Vir, and 7 Psc. As stated by Heiter et al. (2015), the fundamental T_{eff} value for the stars ϵ Vir and μ Leo is significantly lower (~ 3 percent) than the value derived in spectroscopic studies. Lastly, at the hot regime, the typical spectroscopic T_{eff} values computed for the star HD 49933 are generally larger.

Lastly, in Fig. 15, we show the final Fe I and Fe II abundances versus the excitation potential and the reduced EW of the lines, for the four reference CARMENES spectra (18 Sco, μ Cas, ϵ Vir, and Arcturus).

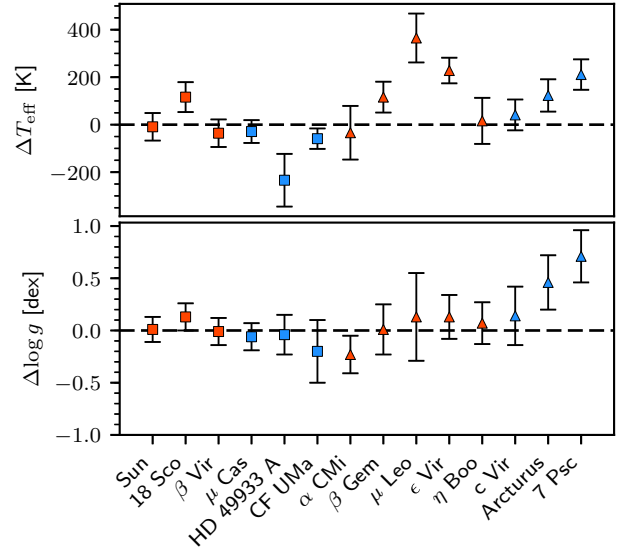


Figure 14. Differences in T_{eff} and $\log g$ between this work and Heiter et al. (2015), with updated values from Jofré et al. (2018), for the *Gaia* benchmark stars in our sample. Symbols are the same as in Fig. 1.

5 CONCLUSIONS

In this work, we have expanded previous optical Fe I and Fe II line lists into the wavelength range covered by CARMENES, i.e. from 5300 to 17 100 Å. The line lists are suited for FGK-type stars and relate to MRDs, MPDs, MRGs, and MPGs. For the first time, we provide Fe I and Fe II lines in the wavelength region between 6800 and 10 000 Å. Altogether, these new line lists contain 653 Fe I and 23 Fe II lines, of which 351 and eight are new additions to the line lists compiled in Tabernero et al. (2019), respectively. This implies more than doubling the number of Fe I and Fe II lines useful for abundance and radial-velocity analyses. The availability of these Fe I and Fe II line lists is also an asset for other new high-resolution near-infrared spectrographs such as SPIRou, GIANO, CRIRES+, IRD, HPF, and NIRPS that also provide wavelength coverage in the near-infrared wavelength region.

We have reported that the star c Gem (HD 62285) is a new SB2 system, as shown by the cross-correlation with an atlas spectrum of Arcturus.

In addition, we have computed a homogenized set of stellar atmospheric parameters for a sample of 65 FGK-type stars observed with CARMENES by means of the EW method. We made a comprehensive comparison of our T_{eff} , $\log g$, and $[\text{Fe}/\text{H}]$ values with those of virtually all relevant determinations of stellar atmospheric parameters of FGK-type stars. Our parameter determinations are in good agreement with the literature values in general, particularly with the region of the parameter space covered by the *YaPSI* isochrones (Spada et al. 2017) and the *Gaia* benchmark stars (Jofré et al. 2014, 2018; Heiter et al. 2015). The scarcity of Fe II lines in the NIR wavelength range covered by CARMENES prevented us from performing the stellar parameter determinations using this spectral region alone. However, when using both VIS and NIR CARMENES channel data, we found a broader T_{eff} scale that seems to be linked to a higher sensitivity to effective temperature of the iron lines found in the NIR region.

The line selections provided in this work will be useful for the spectroscopic analysis of any FGK-type star simultaneously observed in the optical and near-infrared wavelength regions. Finally,

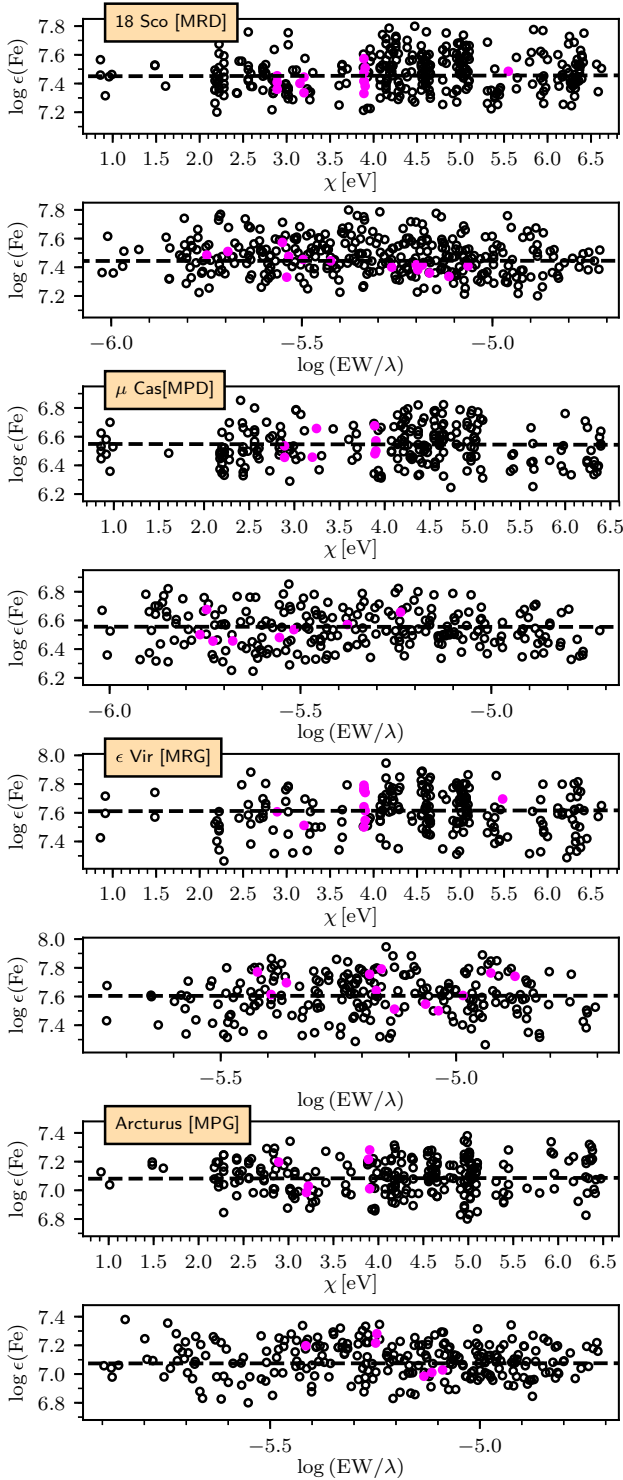


Figure 15. From top to bottom: line iron abundance retrieved by STEPAR for the final solution of the four reference stars: 18 Sco, μ Cas, ϵ Vir, and Arcturus. $\log \epsilon(\text{Fe I})$ stands for the Fe abundance returned by the Fe I lines, whereas the pink dots are Fe II lines. The dashed black lines represent the least-squares fit to the data points.

in a forthcoming publication we plan to expand optical line lists of additional chemical species into the NIR covered by CARMENES and thus assess the impact of the near-infrared wavelength region upon chemical abundance computations for FGK-type stars.

ACKNOWLEDGEMENTS

CARMENES is an instrument for the Centro Astronómico Hispano en Andalucía at Calar Alto (CAHA). CARMENES is funded by the German Max-Planck Gesellschaft (MPG), the Spanish Consejo Superior de Investigaciones Científicas (CSIC), the European Union through FEDER/ERF FICTS-2011-02 funds, and the members of the CARMENES Consortium (Max-Planck-Institut für Astronomie, Instituto de Astrofísica de Andalucía, Landessternwarte Königstuhl, Institut de Ciències de l'Espai, Institut für Astrophysik Göttingen, Universidad Complutense de Madrid, Thüringer Landessternwarte Tautenberg, Instituto de Astrofísica de Canarias, Hamburger Sternwarte, Centro de Astrobiología and Centro Astronómico Hispano en Andalucía), with additional contributions by the Ministerio de Asuntos Económicos y Transformación Digital, the German Research Foundation (DFG) through the Major Research Instrumentation Programme and DFG Research Unit FOR2544 ‘Blue Planets around Red Stars’, the Klaus Tschira Stiftung, the states of Baden-Württemberg and Niedersachsen, and by the Junta de Andalucía. The authors acknowledge financial support from the Fundação para a Ciência e a Tecnologia (FCT) through national funds (PTDC/FIS-AST/28953/2017) and by Fundo Europeu de Desenvolvimento Regional (FEDER) through COMPETE2020 – Programa Operacional Competitividade e Internacionalização (POCI-01-0145-FEDER-028953), the Ministerio de Ciencia e Innovación through fellowship FPU15/01476, and projects AYA2016-79425-C3-1/2/3-P, and the Universidad Complutense de Madrid. JIGH acknowledges financial support from the Ministerio de Ciencia e Innovación under the 2013 Ramón y Cajal programme RYC-2013-14875, and from the project AYA2017-86389-P. This work has made use of the VALD database, operated at Uppsala University, the Institute of Astronomy RAS in Moscow, and the University of Vienna. We thank Calar Alto Observatory for the allocation of director’s discretionary time to this programme. EM would also like to warmly thank the staff at the Hamburger Sternwarte for their hospitality during his stay funded by project EST18/00162 from the Ministerio de Ciencia e Innovación. Based on data from the CARMENES data archive at CAB (INTA-CSIC).

REFERENCES

- Adibekyan V. Z., González Hernández J. I., Delgado Mena E., Sousa S. G., Santos N. C., Israelian G., Figueira P., Bertran de Lis S., 2014, *A&A*, 564, L15
- Allende Prieto C., Barklem P. S., Lambert D. L., Cunha K., 2004, *A&A*, 420, 183
- Allende Prieto C. et al., 2008, *Astron. Nachr.*, 329, 1018
- Andreasen D. T., Sousa S. G., Delgado Mena E., Santos N. C., Tsantaki M., Rojas-Ayala B., Neves V., 2016, *A&A*, 585, A143
- Artigau É. et al., 2014, in Ramsay S. K., McLean I. S., Takami H., eds, *Proceedings SPIE Conference Series*, Vol. 9147, Ground-based and Airborne Instrumentation for Astronomy V, *Proceedings SPIE Conference Series*, Bellingham, p. 914715
- Aurière M., 2003, in Arnaud J., Meunier N., eds, *EAS Publ. Ser. Vol. 9, Magnetism and Activity of the Sun and Stars*. Cambridge Univ. Press, Cambridge, p. 105
- Bensby T., Feltzing S., Oey M. S., 2014, *A&A*, 562, A71
- Blanco-Cuaresma S., 2019, *MNRAS*, 486, 2075

- Blanco-Cuaresma S., Soubiran C., Heiter U., Jofré P., 2014, *Astrophysics Source Code Library*, record ascl:1409.006
- Caballero J. A. et al., 2016, in Peck A. B., Seaman R. L., Benn C. R., eds, *Proc. SPIE Conf. Ser. Vol. 9910, Observatory Operations: Strategies, Processes, and Systems VI*. SPIE, Bellingham, p. 99100E
- Clough S. A., Shephard M. W., Mlawer E. J., Delamere J. S., Iacono M. J., Cady-Pereira K., Boukabara S., Brown P. D., 2005, *J. Quant. Spectrosc. Radiat. Transfer*, 91, 233
- da Silva L. et al., 2006, *A&A*, 458, 609
- da Silva R., Milone A. d. C., Rocha-Pinto H. J., 2015, *A&A*, 580, A24
- De Medeiros J. R., do Nascimento J. D. J., Sankarankutty S., Costa J. M., Maia M. R. G., 2000, *A&A*, 363, 239
- De Medeiros J. R., Udry S., Burki G., Mayor M., 2002, *A&A*, 395, 97
- De Silva G. M. et al., 2015, *MNRAS*, 449, 2604
- Delgado Mena E. et al., 2018, *A&A*, 619, A2
- dos Santos L. A. et al., 2016, *A&A*, 592, A156
- Famaey B., Jorissen A., Luri X., Mayor M., Udry S., Dejonghe H., Turon C., 2005, *A&A*, 430, 165
- Gaia Collaboration, 2018, *A&A*, 616, A1
- Gilmore G. et al., 2012, *The Messenger*, 147, 25
- Girard T. M. et al., 2000, *AJ*, 119, 2428
- Gontcharov G. A., 2006, *Astron. Lett.*, 32, 759
- Gordon I. E., Rothman L. S., Tan Y., Kochanov R. V., Hill C., 2017, 72nd International Symposium on Molecular Spectroscopy, p. TJ08
- Gray D. F., 2018, *ApJ*, 869, 81
- Gray D. F., Toner C. G., 1986, *ApJ*, 310, 277
- Gustafsson B., Edvardsson B., Eriksson K., Jørgensen U. G., Nordlund Å., Plez B., 2008, *A&A*, 486, 951
- Hatzes A., CRIRES + Team, 2017, American Astronomical Society Meeting Abstracts #230, p. 117.02
- Hayes C. R. et al., 2018, *ApJ*, 852, 49
- Heiter U., Luck R. E., 2003, *AJ*, 126, 2015
- Heiter U., Jofré P., Gustafsson B., Korn A. J., Soubiran C., Thévenin F., 2015, *A&A*, 582, A49
- Hekker S., Meléndez J., 2007, *A&A*, 475, 1003
- Hinkle K., Wallace L., Valenti J., Harmer D., 2000, *Visible and Near Infrared Atlas of the Arcturus Spectrum 3727–9300 Å*, Astronomical Society of the Pacific, San Francisco
- Jofré P. et al., 2014, *A&A*, 564, A133
- Jofré E., Petrucci R., Saffe C., Saker L., de la Villarmois E. A., Chavero C., Gómez M., Mauas P. J. D., 2015, *A&A*, 574, A50
- Jofré P., Heiter U., Tucci Maia M., Soubiran C., Worley C. C., Hawkins K., Blanco-Cuaresma S., Rodrigo C., 2018, *Res. Notes Am. Astron. Soc.*, 2, 152
- Jofré P., Heiter U., Soubiran C., 2019, *ARA&A*, 57, 5
- Karataş Y., Bilir S., Eker Z., Demircan O., 2004, *MNRAS*, 349, 1069
- Kasting J. F., Whitmire D. P., Reynolds R. T., 1993, *Icarus*, 101, 108
- Kausch W. et al., 2015, *A&A*, 576, A78
- Keenan P. C., McNeil R. C., 1989, *ApJS*, 71, 245
- Kopparapu R. K. et al., 2013, *ApJ*, 765, 131
- Kotani T. et al., 2014, in Ramsay S. K., McLean I. S., Takami H., eds, *Proc. SPIE Conf. Ser. Vol. 9147, Ground-based and Airborne Instrumentation for Astronomy V*. SPIE, Bellingham, p. 914714
- Kupka F., Piskunov N., Ryabchikova T. A., Stempels H. C., Weiss W. W., 1999, *A&AS*, 138, 119
- Kupka F. G., Ryabchikova T. A., Piskunov N. E., Stempels H. C., Weiss W. W., 2000, *Balt. Astron.*, 9, 590
- Lèbre A., de Laverny P., Do Nascimento J. D. J., de Medeiros J. R., 2006, *A&A*, 450, 1173
- Lebzelter T. et al., 2012, *A&A*, 539, A109
- Liu Y. J., Zhao G., Shi J. R., Pietrzyński G., Gieren W., 2007, *MNRAS*, 382, 553
- Luck R. E., 2014, *AJ*, 147, 137
- Lyubimkov L. S., Lambert D. L., Rostopchin S. I., Rachkovskaya T. M., Poklad D. B., 2010, *MNRAS*, 402, 1369
- Lyubimkov L. S., Lambert D. L., Kaminsky B. M., Pavlenko Y. V., Poklad D. B., Rachkovskaya T. M., 2012, *MNRAS*, 427, 11
- Majewski S. R. et al., 2017, *AJ*, 154, 94
- Maldonado J., Martínez-Arnáiz R. M., Eiroa C., Montes D., Montesinos B., 2010, *A&A*, 521, A12
- Mann A. W. et al., 2019, *ApJ*, 871, 63
- Martínez-Arnáiz R., Maldonado J., Montes D., Eiroa C., Montesinos B., 2010, *A&A*, 520, A79
- Massarotti A., Latham D. W., Stefanik R. P., Fogel J., 2008, *AJ*, 135, 209
- Mayor M. et al., 2003, *The Messenger*, 114, 20
- McCarthy K., Wilhelm R. J., 2014, *AJ*, 148, 70
- McWilliam A., 1990, *ApJS*, 74, 1075
- Meléndez J., Barbuy B., 2009, *A&A*, 497, 611
- Montes D. et al., 2018, *MNRAS*, 479, 1332
- Morel T. et al., 2014, *A&A*, 564, A119
- Morton D. C., 2000, *ApJS*, 130, 403
- Mucciarelli A., Pancino E., Lovisi L., Ferraro F. R., Lapenna E., 2013, *ApJ*, 766, 78
- Nicholls C. P. et al., 2017, *A&A*, 598, A79
- Nidever D. L., Marcy G. W., Butler R. P., Fischer D. A., Vogt S. S., 2002, *ApJS*, 141, 503
- Oliva E., Sanna N., Rainer M., Massi F., Tozzi A., Origlia L., 2018, in Evans C. J., Simard L., Takami H., eds, *Proc. SPIE Conf. Ser. Vol. 7015, Ground-based and Airborne Instrumentation for Astronomy VII*. SPIE, Bellingham, p. 1070274
- Origlia L. et al., 2014, in Ramsay S. K., McLean I. S., Takami H., eds, *Proc. SPIE Conf. Ser. Vol. 9147, Ground-based and Airborne Instrumentation for Astronomy V*. SPIE, Bellingham, p. 91471E
- Park S. et al., 2018, *ApJS*, 238, 29
- Passegger V. M. et al., 2019, *A&A*, 627, A161
- Pavlenko Y. V., Jenkins J. S., Jones H. R. A., Ivanyuk O., Pinfield D. J., 2012, *MNRAS*, 422, 542
- Piskunov N. E., Valenti J. A., 2002, *A&A*, 385, 1095
- Piskunov N., Valenti J. A., 2017, *A&A*, 597, A16
- Piskunov N. E., Kupka F., Ryabchikova T. A., Weiss W. W., Jeffery C. S., 1995, *A&AS*, 112, 525
- Pourbaix D. et al., 2004, *A&A*, 424, 727
- Press W. H., Teukolsky S. A., Vetterling W. T., Flannery B. P., 2002, *Numerical Recipes in C++ : The Art of Scientific Computing*. Cambridge Univ. Press, Cambridge
- Quirrenbach A. et al., 2018, in Evans C. J., Simard L., Takami H., eds, *Proc. SPIE Conf. Ser. Vol. 10702, Ground-based and Airborne Instrumentation for Astronomy VII*. SPIE, Bellingham, p. 107020W
- Reiners A. et al., 2018, *A&A*, 612, A49
- Rodrigues T. S. et al., 2014, *MNRAS*, 445, 2758
- Rodrigues T. S. et al., 2017, *MNRAS*, 467, 1433
- Ryabchikova T., Piskunov N., Kurucz R. L., Stempels H. C., Heiter U., Pakhomov Y., Barklem P. S., 2015, *Phys. Scr.*, 90, 054005
- Santos N. C. et al., 2013, *A&A*, 556, A150
- Scarfe C. D., Funakawa H., Delaney P. A., Barlow D. J., 1983, *J. R. Astron. Soc. Can.*, 77, 126
- Schweitzer A. et al., 2019, *A&A*, 625, A68
- Skrutskie M. F. et al., 2006, *AJ*, 131, 1163
- Smette A. et al., 2015, *A&A*, 576, A77
- Snedden C. A., 1973, PhD thesis, The University of Texas at Austin
- Soubiran C., Jasiewicz G., Chemin L., Crifo F., Udry S., Hestroffer D., Katz D., 2013, *A&A*, 552, A64
- Soubiran C., Le Campion J.-F., Brouillet N., Chemin L., 2016, *A&A*, 591, A118
- Sousa S. G., Santos N. C., Israelian G., Mayor M., Monteiro M. J. P. F. G., 2007, *A&A*, 469, 783
- Sousa S. G. et al., 2008, *A&A*, 487, 373
- Spada F., Demarque P., Kim Y.-C., Boyajian T. S., Brewer J. M., 2017, *ApJ*, 838, 161
- Spencer Jones H., Furner H. H., 1937, *MNRAS*, 98, 92
- Steinmetz M. et al., 2006, *AJ*, 132, 1645
- Taberner H. M., Montes D., González Hernández J. I., 2012, *A&A*, 547, A13
- Taberner H. M., Montes D., González Hernández J. I., Ammler-von Eiff M., 2017, *A&A*, 597, A33

- Tabernero H. M., Dorda R., Negueruela I., González-Fernández C., 2018, *MNRAS*, 476, 3106
- Tabernero H. M., Marfil E., Montes D., González Hernández J. I., 2019, *A&A*, 628, A131
- Takeda Y. et al., 2005, *PASJ*, 57, 13
- Takeda Y., Sato B., Murata D., 2008, *PASJ*, 60, 781
- Thygesen A. O. et al., 2012, *A&A*, 543, A160
- Tsantaki M., Sousa S. G., Adibekyan V. Z., Santos N. C., Mortier A., Israelian G., 2013, *A&A*, 555, A150
- Valenti J. A., Fischer D. A., 2005, *ApJS*, 159, 141
- van Leeuwen F., 2007, *A&A*, 474, 653
- Wildi F. et al., 2017, Shaklan S., ed., Proc. SPIE Conf. Ser. Vol. 10400, Techniques and Instrumentation for Detection of Exoplanets VIII. SPIE, Bellingham, p. 1040018
- Worek T. F., Beardsley W. R., 1977, *ApJ*, 217, 134
- Wright J. T. et al., 2018, American Astronomical Society Meeting Abstracts #231, p. 246.45
- Wu Y., Singh H. P., Prugniel P., Gupta R., Koleva M., 2011, *A&A*, 525, A71
- Zamora O. et al., 2015, *AJ*, 149, 181
- Zechmeister M., Anglada-Escudé G., Reiners A., 2014, *A&A*, 561, A59

SUPPORTING INFORMATION

Supplementary data are available at *MNRAS* online.

Fig. A1. CARMENES spectrum of 18 Sco.

Table A2. Stellar atmospheric parameters of the selected sample under STEPAR and $\log g$ values obtained with PARAM assuming parallaxes from Gaia DR2 and the *Hipparcos* mission.

Table A3. Stellar atmospheric parameters of the selected sample under STEPAR restricted to the optical and $\log g$ values obtained with PARAM assuming parallaxes from Gaia DR2 and the *Hipparcos* mission.

Please note: Oxford University Press is not responsible for the content or functionality of any supporting materials supplied by the authors. Any queries (other than missing material) should be directed to the corresponding author for the article.

APPENDIX A: APPENDIX

In Table A1, we give the literature values of the stellar atmospheric parameters for the selected sample. In Tables A2 and A3, we give the stellar atmospheric parameters computed with STEPAR in the whole VIS + NIR region and VIS region, respectively. In Tables A4 and A5, we list the Fe I and Fe II lines along with their parameters, respectively, for MRDs, MPDs, MRGs, and MPGs. Finally, we include the CARMENES spectrum of the reference, MRD 18 Sco in Fig. A6, along with the Fe I and Fe II lines indicated in red and green, respectively.

Table A1. Reference stellar parameters of the selected CARMENES sample.

Name	HD	α (J2000)	δ (J2000)	π [mas]	Ref. ^a	SpT ^b	v_t [km s ⁻¹]	Ref. ^c	$v \sin i$ [km s ⁻¹]	Ref. ^d	T_{eff} [K]	$\log g$ [dex]	ξ [km s ⁻¹]	[Fe/H] [dex]	Ref. ^e
Metal-rich dwarfs (MRD)															
Sun ^f	—	—	—	—	—	G2 V	0.00	—	1.6	Pav12	5771 ± 1	4.44 ± 0.00	1.20 ± 0.18	+0.03 ± 0.05	Jof18
HD 3765	3765	00 40 49.29	+40 11 13.3	55.7562 ± 0.1002	G	K2 V	−63.11	Sou13	9.2	Mar10	5032 ± 44	4.59 ± 0.06	0.85 ± —	+0.18 ± 0.03	Val05
HD 100167	100167	11 31 53.92	+41 26 21.5	28.4793 ± 0.1513	G	F8 V	−29.49	Nid02	5.0	McC14	5915 ± 44	4.38 ± 0.06	0.85 ± —	+0.06 ± 0.03	Val05
61 UMa	101501	11 41 03.01	+34 12 06.4	104.3904 ± 0.1287	G	G8 V	−5.18	Nid02	3.3	Mar10	5488 ± 44	4.43 ± 0.06	0.85 ± —	−0.03 ± 0.03	Val05
β Vir ^f	102870	11 50 41.73	+01 45 52.8	89.9258 ± 0.5195	G	F9 V	+6.71	Nid02	3.4	Mar10	6083 ± 41	4.10 ± 0.02	1.40 ± 0.09	+0.24 ± 0.07	Jof18
β CVn	109358	12 33 44.54	+41 21 27.0	116.1298 ± 0.6776	G	G0 V	+6.52	Nid02	3.2	Mar10	5930 ± 44	4.44 ± 0.06	0.85 ± —	−0.16 ± 0.03	Val05
β Com	114710	13 11 52.38	+27 52 41.1	108.8951 ± 0.3487	G	F9.5 V	+5.46	Nid02	4.7	Mar10	6075 ± 44	4.57 ± 0.06	0.85 ± —	+0.07 ± 0.03	Val05
ξ Boo	131156	14 51 23.28	+19 06 03.4	148.5195 ± 0.2436	G	G7 Ve +	+1.59	Kar04	3.3	Mar10	5570 ± 44	4.65 ± 0.06	0.85 ± —	−0.04 ± 0.03	Val05
λ Ser	141004	15 46 26.61	+07 21 10.9	84.6121 ± 0.2559	G	G0 IV–V	−66.07	Nid02	3.2	Mar10	5936 ± 44	4.30 ± 0.06	0.85 ± —	+0.05 ± 0.03	Val05
18 Sco ^f	146233	16 15 37.26	−08 22 09.6	70.7675 ± 0.1119	G	G2 Va	+11.90	Gaia	2.1	San16	5810 ± 80	4.44 ± 0.03	1.20 ± 0.20	+0.03 ± 0.03	Jof18
HD 166620	166620	18 09 37.45	+38 27 28.8	90.1264 ± 0.0200	G	K2 V	−19.47	Sou13	4.8	Mar10	5000 ± 44	4.47 ± 0.06	0.85 ± —	−0.18 ± 0.03	Val05
HD 182488	182488	19 23 34.01	+33 13 19.1	64.0623 ± 0.0218	G	G9 V	−21.47	Sou13	0.6	Fek97	5453 ± 44	4.67 ± 0.06	0.85 ± —	+0.22 ± 0.03	Val05
σ Dra	185144	19 32 21.53	+69 39 41.3	173.2405 ± 0.2070	G	G9 V	+26.78	Nid02	6.8	Mar10	5218 ± 96	4.61 ± 0.05	1.07 ± —	−0.25 ± 0.02	All04
HD 219134	219134	23 13 16.92	+57 10 05.9	153.0808 ± 0.0895	G	K3 V	−18.83	Nid02	6.9	Mar10	4743 ± 86	4.63 ± 0.04	1.00 ± —	+0.12 ± 0.02	All04
Metal-poor dwarfs (MPD)															
η Cas	4614	00 49 06.22	+57 48 54.5	171.2861 ± 0.5815	G	F9 V +	+8.44	Nid02	3.2	Mar10	5900 ± 50	4.50 ± 0.05	0.90 ± 0.05	−0.35 ± 0.04	Hei03
μ Cas ^f	6582	01 08 15.97	+54 55 14.8	132.38 ± 0.82	H	K1 V	−98.10	Pou04	4.2	Mar10	5308 ± 29	4.41 ± 0.06	1.10 ± 0.29	−0.81 ± 0.03	Jof18
HD 49933 ^f	49933	06 50 49.83	−00 32 27.0	33.4441 ± 0.0891	G	F3 V	−12.65	Gaia	5.0	Tak05	6635 ± 91	4.20 ± 0.03	1.90 ± 0.35	−0.41 ± 0.08	Jof18
CF UMa ^f	103095	11 52 58.80	+37 43 06.0	108.9551 ± 0.0490	G	G8 Vp	−97.49	Hay18	9.3	Mar10	5140 ± 55	4.60 ± 0.03	1.10 ± 0.57	−1.46 ± 0.39	Jof18
HD 154363	154363	17 03 07.86	+14 05 31.0	95.5499 ± 0.0651	G	K4 V	+34.22	Mon18	1.9	Mar10	4723 ± 89	4.41 ± 0.24	—	−0.62 ± 0.04	Sou08
Metal-rich giants (MRG)															
ι Gem	58207	07 25 43.59	+27 47 52.9	24.8793 ± 0.3562	G	G9 IIIb	+7.26	Mas08	0.0	Mas08	4912 ± 56	2.82 ± 0.28	1.47 ± 0.09	−0.03 ± 0.10	Sill15
α CMi ^f	61421	07 39 18.05	+05 13 29.8	284.56 ± 1.26	H	F5 IV–V	−4.10	Mal10	5.4	Mar10	6554 ± 84	4.00 ± 0.02	1.80 ± 0.11	+0.01 ± 0.08	Jof18
κ Gem	62345	07 44 26.84	+24 23 52.6	23.6199 ± 0.3954	G	G8 IIIa	+20.15	Sou08	3.3	Mas08	5120 ± 28	2.98 ± 0.16	1.56 ± 0.04	+0.03 ± 0.05	Sill15
β Gem ^f	62509	07 45 18.91	+28 01 34.0	96.54 ± 0.27	H	K0 IIIb	+3.23	Jof15	2.3	Jof15	4858 ± 60	2.90 ± 0.08	1.10 ± 0.21	+0.13 ± 0.16	Jof18
ζ Mon	67594	08 08 35.65	−02 59 01.5	4.7723 ± 0.3259	G	G2 Iab/b	+31.20	Gaia	6.7	Med02	5210 ± 100	1.75 ± 0.07	3.3 ± 0.5	+0.01 ± 0.12	Lyu10
β Cnc	69267	08 16 30.90	+09 11 08.0	11.0443 ± 0.6561	G	K4 III	+22.94	Fam05	6.9	Mas08	4200 ± —	2.05 ± —	2.30 ± —	−0.19 ± —	Hei07
F Hy ^a	74395	08 43 40.37	−07 14 01.2	1.8273 ± 0.2985	G	G0/2 Ib	+27.68	Gaia	7.5	Med02	5370 ± 100	2.08 ± 0.06	3.5 ± 0.5	−0.03 ± 0.13	Lyu10
ζ Hy ^a	76294	08 55 23.62	+05 56 44.1	20.7182 ± 0.3925	G	G9 II–III	+22.30	Gon06	2.5	Mas08	5049 ± 55	2.88 ± 0.30	1.67 ± 0.08	+0.01 ± 0.11	Sill15
HD 77912	77912	09 06 31.77	+38 27 08.0	5.0045 ± 0.1977	G	G7 II	+16.04	Gaia	1.5	Med02	5001 ± —	2.03 ± —	2.16 ± —	+0.12 ± —	Luc14
α Hy ^a	81797	09 27 35.24	−08 39 30.8	18.09 ± 0.18	H	K3 IIIa	−4.27	Jof15	4.0	Jof15	4395 ± 37	2.09 ± 0.11	1.76 ± 0.12	−0.11 ± 0.05	Jof15
DK UMa	82210	09 34 28.88	+69 49 49.0	30.9269 ± 0.1621	G	G5 III–IV	−27.07	Gaia	5.5	Med00	5343 ± 33	3.49 ± 0.08	—	−0.21 ± 0.07	Wul11
10 LMi	82635	09 34 13.38	+36 23 51.3	18.1458 ± 0.2345	G	G8.5 III	−11.94	Mas08	6.5	Mas08	5195 ± 40	3.26 ± 0.26	1.56 ± 0.06	−0.02 ± 0.07	Sill15
ϵ Leo	84441	09 45 51.08	+23 46 27.3	11.1759 ± 0.9166	G	G1 II	+4.48	Sou08	8.1	Mas08	5383 ± —	2.17 ± —	2.09 ± —	+0.04 ± —	Luc14
μ Leo ^f	85503	09 52 45.85	+26 00 24.8	30.6493 ± 0.4219	G	K2 III	+13.63	Fam05	4.5	Mas08	4474 ± 60	2.51 ± 0.11	—	+0.25 ± 0.15	Jof18
β LMi	90537	10 27 53.02	+36 42 25.9	21.19 ± 0.50	H	G9 IIIb	+8.52	Gaia	7.1	Mas08	5060 ± —	2.95 ± —	2.1 ± —	0.00 ± 0.10	McW90
37 LMi	92125	10 38 43.21	+31 58 34.6	5.2136 ± 0.4108	G	G3 Ib–II	−7.71	Gaia	9.5	Lyu12	5475 ± 50	2.36 ± 0.04	2.7 ± 0.5	+0.02 ± 0.11	Lyu10
α UMa	95689	11 03 43.64	+61 45 03.4	26.54 ± 0.48	H	G8 III +	−9.40	Gon06	2.7	Gra18	4660 ± —	2.46 ± —	2.2 ± —	−0.20 ± 0.07	McW90
ψ UMa	96833	11 09 39.79	+44 29 54.4	21.0443 ± 0.5249	G	K1 III	−3.39	Fam05	5.5	Mas08	4600 ± 22	1.95 ± 0.08	—	+0.03 ± 0.08	Thy12
ν UMa	98262	11 18 28.74	+33 05 39.3	14.2521 ± 0.5672	G	K3 III	−9.63	Fam05	2.7	Med00	4120 ± —	1.86 ± —	2.4 ± —	−0.20 ± 0.12	McW90
56 UMa	98839	11 22 49.58	+43 28 57.7	5.8742 ± 0.1937	G	G8 IIIa	+1.01	Pou04	4.0	Leb06	4936 ± 25	2.30 ± 0.08	1.78 ± 0.10	−0.05 ± 0.04	Tak08
ϵ Vir ^f	113226	13 02 10.59	+10 57 32.9	30.5624 ± 0.4379	G	G8 III	−14.29	Jof15	1.4	Jof15	4983 ± 61	2.77 ± 0.02	1.10 ± 0.25	+0.15 ± 0.16	Jof18

Table A1 – continued

pName	HD	α (J2000)	δ (J2000)	π [mas]	Ref. ^a	Spt ^b	v_r [km s ⁻¹]	Ref. ^c	$v \sin i$ [km s ⁻¹]	Ref. ^d	T_{eff} [K]	log g [dex]	ξ [km s ⁻¹]	[Fe/H] [dex]	Ref. ^e
η Boo ^f	121370	13 54 41.06	+18 23 51.4	87.75 \pm 1.24	H	G0IV	-13.70	Jof15	12.3	Jof15	6099 \pm 28	3.79 \pm 0.02	1.92 \pm 0.03	+0.32 \pm 0.08	Jof15
ρ Boo	127665	14 31 49.77	+30 22 16.9	21.9348 \pm 0.3952	G	K3 III	-10.57	Mas08	5.0	Mas08	4258 \pm 65	1.85 \pm 0.36	1.59 \pm 0.12	-0.13 \pm 0.12	Sill5
β UMi	131873	14 50 42.35	+74 09 19.9	24.91 \pm 0.12	H	K4 III	+16.96	Fam05	1.6	Gon99	4067 \pm 13	1.70 \pm 0.11	-	-0.13 \pm 0.05	Wu11
δ Boo	135722	15 15 30.15	+33 18 53.7	26.7797 \pm 0.3806	G	G8 IV	-12.29	Sou08	3.6	Mas08	4982 \pm 28	2.89 \pm 0.19	1.44 \pm 0.04	-0.23 \pm 0.06	Sill5
ι Dra	137759	15 24 55.78	+58 57 57.7	31.5727 \pm 0.2959	G	K2 III	-12.31	Gaia	1.9	Jof15	4504 \pm 16	2.52 \pm 0.07	1.41 \pm 0.07	+0.03 \pm 0.04	Jof15
α Ser	140573	15 44 16.05	+06 25 32.4	39.3696 \pm 0.8514	G	K2 IIIb	-2.63	Fam05	4.3	Mas08	4496 \pm -	2.52 \pm -	1.5 \pm 0.2	+0.17 \pm -	Liu07
κ CrB	142091	15 51 13.94	+35 39 26.4	33.2328 \pm 0.1083	G	K0 IIIb–IV	-23.16	Jof15	1.4	Jof15	4803 \pm 25	3.23 \pm 0.04	0.83 \pm 0.06	+0.17 \pm 0.05	Jof15
ϵ CrB	143107	15 57 35.23	+26 52 40.0	14.2898 \pm 0.2149	G	K2 III	-32.42	Fam05	2.4	Mas08	4436 \pm 56	1.94 \pm 0.15	1.68 \pm 0.06	-0.22 \pm 0.03	San13
ϵ Oph	146791	16 18 19.28	-04 41 32.7	30.2620 \pm 0.7915	G	G9.5 IIIb	-9.18	Mas08	3.6	Mas08	4940 \pm 55	2.64 \pm 0.06	1.43 \pm 0.06	-0.04 \pm 0.10	Mor14
ζ Her	150680	16 41 17.28	+31 36 09.3	93.32 \pm 0.47	H	G1 IV	-67.80	Gon06	3.1	Mar10	5655 \pm 148	3.67 \pm 0.12	1.38 \pm -	-0.01 \pm 0.02	AlI04
κ Oph	153210	16 57 40.07	+09 22 29.9	36.8142 \pm 0.4578	G	K2 III	-55.85	Mas08	4.7	Mas08	4655 \pm -	2.70 \pm -	1.82 \pm -	+0.07 \pm -	Hek07
π Her	156283	17 15 02.85	+36 48 32.9	9.1810 \pm 0.4201	G	K3 II	-25.57	Fam05	1.3	Leb06	4170 \pm -	1.90 \pm -	2.26 \pm -	+0.01 \pm -	Hek07
σ Oph	157999	17 26 30.87	+04 08 25.2	3.8431 \pm 0.2836	G	K2 III	-27.81	Fam05	4.2	Leb06	4080 \pm -	1.52 \pm -	2.54 \pm -	-0.07 \pm -	Hek07
β Dra	159181	17 30 25.97	+52 18 05.1	8.1882 \pm 0.5562	G	G2 Ib–IIa	-21.00	Sou08	10.7	Leb06	5160 \pm 150	1.86 \pm 0.04	3.0 \pm 0.5	+0.02 \pm 0.10	Lyu10
β Oph	161096	17 43 28.35	+04 34 02.2	40.0945 \pm 0.6752	G	K2 III	-12.53	Fam05	5.4	Mas08	4680 \pm -	2.95 \pm -	2.02 \pm -	+0.13 \pm -	Hek07
μ Her	161797	17 46 27.52	+27 43 14.2	119.1128 \pm 0.4848	G	G5 IV	-17.69	Mon18	1.7	Jof15	5562 \pm 35	3.98 \pm 0.05	1.02 \pm 0.07	+0.28 \pm 0.05	Jof15
ξ Dra	163588	17 53 31.73	+56 52 21.6	29.8654 \pm 0.3051	G	K2 III	-26.46	Mas08	2.3	Mas08	4702 \pm 76	2.94 \pm 0.33	1.41 \pm 0.21	+0.12 \pm 0.14	Sill5
θ Her	163770	17 56 15.17	+37 15 01.9	2.7547 \pm 0.2684	G	K1 II +	-28.32	Fam05	3.4	Gr86	4255 \pm -	1.25 \pm -	2.75 \pm -	-0.11 \pm -	Hek07
ξ Her	163993	17 57 45.88	+29 14 52.3	25.2599 \pm 0.3303	G	G8 III	-1.72	Fam05	2.8	Mas08	5220 \pm 51	3.28 \pm 0.26	1.62 \pm 0.08	+0.06 \pm 0.09	Sill5
ν Oph	163917	17 59 01.60	-09 46 24.9	23.0524 \pm 0.4626	G	K1 III	+13.19	Jof15	2.8	Jof15	4997 \pm 56	2.84 \pm 0.09	1.60 \pm 0.05	+0.05 \pm 0.07	Jof15
Metal-poor giants (MPG)															
c Vir ^f	107328	12 20 20.99	+03 18 45.3	9.7577 \pm 0.2536	G	K0 IIIb	+36.66	Gaia	1.9	Mas08	4496 \pm 59	2.09 \pm 0.13	1.20 \pm 0.26	-0.33 \pm 0.16	Jof18
ν Boo	120477	13 49 28.67	+15 47 52.3	14.2758 \pm 0.3494	G	K5.5 III	-5.85	Fam05	5.1	Mas08	4170 \pm -	1.60 \pm -	2.60 \pm -	-0.57 \pm -	Hek07
Arcurus ^f	124897	14 15 39.68	+19 10 55.8	88.83 \pm 0.54	H	K1.5 III	-5.19	Mas08	4.2	Mas08	4286 \pm 35	1.60 \pm 0.20	1.30 \pm 0.12	-0.52 \pm 0.08	Jof18
γ Lib	138905	15 35 31.57	-14 47 22.2	21.0823 \pm 0.4010	G	G8.5 III	-26.71	Jof15	1.6	Jof15	4786 \pm 13	2.55 \pm 0.04	1.36 \pm 0.05	-0.30 \pm 0.03	Jof15
7 Psc ^f	220009	23 20 20.58	+05 22 52.8	9.5042 \pm 0.1880	G	K1 IV	+40.46	Gaia	1.0	Mcd00	4266 \pm 60	1.43 \pm 0.12	1.30 \pm 0.14	-0.74 \pm 0.13	Jof14

^aReferences for parallax, π : G:Gaia DR2 (Gaia Collaboration 2018); H: Hipparcos (van Leeuwen 2007).^bReference for spectral type, Spt: Caballero et al. (in preparation).^cReference for v_r : Fam05: Famaey et al. (2005); Gaia: Gaia Collaboration (2018); Gon06: Gontcharov (2006); Hay18: Hayes et al. (2018); Kar04: Karaaş et al. (2004); Jof15: Jofré et al. (2015); Mal10: Maldonado et al. (2010); Mas08: Massarotti et al. (2008); Mon18: Montes et al. (2018); Nid02: Nidever et al. (2002); Pou04: Pourbaix et al. (2004); Sou13: Soubiran et al. (2013).^dReference for $v \sin i$: San16: dos Santos et al. (2016); Jof15: Jofré et al. (2015); Gra86: Gray & Toner (1986); Leb06: Lebre et al. (2006); Lyu12: Lyubimkov et al. (2012); Mar10: Martínez-Arriáz et al. (2010); Mas08: Massarotti et al. (2008); McCl14: McCarthy & Wilhelm (2014); Med00: De Medeiros et al. (2000); Med02: De Medeiros et al. (2002); Pav12: Pavlenko et al. (2012); Tak05: Takeda et al. (2005).^eReferences for T_{eff} , log g , ξ , and [Fe/H]: AlI04: Allende Prieto et al. (2004); Hei03: Heiter & Luck (2003); Hek07: Hekker & Meléndez (2007); Jof14: Jofré et al. (2014); Jof15: Jofré et al. (2015); Jof18: Jofré et al. (2018); Liu07: Liu et al. (2007); Luc14: Luck (2014); Lyu10: Lyubimkov et al. (2010); McW90: McWilliam (1990); Mor14: Morel et al. (2014); San13: Santos et al. (2013); Sill5: da Silva et al. (2015); Sou08: Sousa et al. (2008); Tak08: Takeda et al. (2008); Thy12: Thygesen et al. (2012); Val05: Valenti & Fischer (2005); Wu11: Wu et al. (2011).^fGaia benchmark star (Jofré et al. 2014, 2018; Heiter et al. 2015).

Table A2. Stellar atmospheric parameters of the selected sample under STEPAR and $\log g$ values obtained with PARAM assuming parallaxes from Gaia DR2 and the *Hipparcos* mission.

Name	v_r [km s ⁻¹]	S/N	T_{eff} [K]	$\log g$ [dex]	$\log g_{\text{PARAM}}$ [dex]	ξ [km s ⁻¹]	[Fe/H] [dex]
Metal-rich dwarfs (MRD)							
Sun	0.00 ± 0.00	249	5768 ± 58	4.45 ± 0.12	–	1.31 ± 0.09	–0.01 ± 0.04
HD 3765	–63.18 ± 0.50	138	5310 ± 81	4.63 ± 0.24	4.55 ± 0.02	1.43 ± 0.10	+0.12 ± 0.03
HD 100167	–29.41 ± 0.52	98	5898 ± 57	4.47 ± 0.12	4.43 ± 0.02	1.27 ± 0.09	+0.01 ± 0.04
61 UMa	–5.47 ± 0.46	248	5555 ± 59	4.59 ± 0.13	4.52 ± 0.02	1.36 ± 0.10	–0.07 ± 0.03
β Vir	+4.58 ± 0.65	345	6199 ± 63	4.23 ± 0.13	4.09 ± 0.02	1.53 ± 0.08	+0.17 ± 0.04
β CVn	+6.34 ± 0.49	241	5902 ± 61	4.41 ± 0.13	4.37 ± 0.03	1.22 ± 0.10	–0.20 ± 0.04
β Com	+5.41 ± 0.57	198	6000 ± 58	4.44 ± 0.12	4.42 ± 0.01	1.30 ± 0.08	+0.04 ± 0.04
ξ Boo	+1.81 ± 0.40	67	5403 ± 52	4.48 ± 0.12	4.54 ± 0.02	1.45 ± 0.08	–0.19 ± 0.03
λ Ser	–66.22 ± 0.60	109	5835 ± 54	4.00 ± 0.14	4.22 ± 0.02	1.34 ± 0.07	–0.04 ± 0.04
18 Sco	+11.93 ± 0.59	298	5774 ± 58	4.43 ± 0.13	4.41 ± 0.04	1.30 ± 0.08	0.00 ± 0.04

Table A3. Stellar atmospheric parameters of the selected sample under STEPAR restricted to the optical and $\log g$ values obtained with PARAM assuming parallaxes from Gaia DR2 and the *Hipparcos* mission.

Name	v_r [km s ⁻¹]	S/N	T_{eff} [K]	$\log g$ [dex]	$\log g_{\text{PARAM}}$ [dex]	ξ [km s ⁻¹]	[Fe/H] [dex]
Metal-rich dwarfs (MRD)							
Sun	0.00 ± 0.00	249	5787 ± 54	4.42 ± 0.11	–	0.98 ± 0.08	+0.02 ± 0.03
HD 3765	–63.18 ± 0.50	138	5206 ± 84	4.62 ± 0.22	4.55 ± 0.02	1.17 ± 0.12	+0.16 ± 0.04
HD 100167	–29.41 ± 0.52	98	5942 ± 54	4.49 ± 0.10	4.43 ± 0.02	1.04 ± 0.09	+0.04 ± 0.04
61 UMa	–5.47 ± 0.46	248	5576 ± 56	4.56 ± 0.12	4.52 ± 0.02	1.07 ± 0.09	–0.01 ± 0.03
β Vir	+4.58 ± 0.65	345	6255 ± 64	4.20 ± 0.12	4.09 ± 0.02	1.45 ± 0.08	+0.23 ± 0.04
β CVn	+6.34 ± 0.49	241	5967 ± 57	4.40 ± 0.12	4.37 ± 0.03	0.96 ± 0.09	–0.14 ± 0.04
β Com	+5.41 ± 0.57	198	6105 ± 56	4.42 ± 0.11	4.42 ± 0.01	1.18 ± 0.07	+0.02 ± 0.04
ξ Boo	+1.81 ± 0.40	67	5536 ± 55	4.50 ± 0.12	4.54 ± 0.02	1.25 ± 0.09	–0.15 ± 0.03
λ Ser	–66.22 ± 0.60	109	5950 ± 56	4.31 ± 0.14	4.22 ± 0.02	1.22 ± 0.08	+0.05 ± 0.04
18 Sco	+11.93 ± 0.59	298	5786 ± 54	4.40 ± 0.10	4.41 ± 0.04	0.99 ± 0.09	+0.02 ± 0.04

Table A4. Merged Fe I line lists.

λ_{air} [Å]	χ_1 [eV]	$\log gf$	Line list ^a				Reference ^b
			MRD	MPD	MRG	MPG	
5307.361	1.61	−2.912	•	•		•	Sou08
5321.108	4.44	−1.089				•	Sou08
5322.041	2.28	−2.802	•			•	Sou08
5339.929	3.27	−0.635				•	Sou08
5364.871	4.45	+0.228			•	•	Sou08
5373.709	4.47	−0.710	•	•			Sou08
5379.574	3.70	−1.514	•	•	•	•	Sou08
5386.333	4.15	−1.670	•		•	•	Sou08
5389.479	4.42	−0.410		•	•		Sou08
5397.618	3.63	−2.528			•		Sou08
5398.279	4.45	−0.630	•	•	•		Sou08
5400.501	4.37	−0.160	•	•			Sou08
5401.266	4.32	−1.820	•		•		Sou08
5409.133	4.37	−1.200	•	•			Sou08
5417.033	4.42	−1.580	•		•		Sou08
5424.068	4.32	+0.520		•			Sou08
5436.295	4.39	−1.440	•		•	•	Sou08
5436.588	2.28	−2.964			•		Sou08
5441.339	4.31	−1.630	•		•	•	Sou08
5445.042	4.39	−0.020		•	•	•	Sou08
5460.873	3.07	−3.426			•	•	Sou08
5461.550	4.45	−1.800	•		•		Sou08
5463.275	4.44	+0.070			•	•	Sou08
5464.280	4.14	−1.402			•		Sou08
5466.396	4.37	−0.630	•	•		•	Sou08
5470.093	4.45	−1.710	•		•		Sou08
5472.709	4.21	−1.495	•				Sou08
5473.900	4.15	−0.720	•	•			Sou08
5483.099	4.15	−1.392	•			•	Sou08
5501.465	0.96	−3.047		•		•	Sou08
5506.778	0.99	−2.797		•			Sou08
5522.446	4.21	−1.550	•	•			Sou08
5536.580	2.83	−3.810				•	Sou08
5539.280	3.64	−2.660				•	Sou08
5543.147	3.69	−1.570		•			Sou08
5543.935	4.22	−1.140	•	•	•	•	Sou08
5546.505	4.37	−1.310		•			Sou08
5549.949	3.69	−2.910			•		Sou08
5554.894	4.55	−0.440		•			Sou08
5560.211	4.43	−1.190	•	•	•		Sou08
5572.842	3.40	−0.275				•	Sou08
5576.089	3.43	−1.000		•	•	•	Sou08
5618.632	4.21	−1.276	•	•	•	•	Sou08
5619.595	4.39	−1.700	•			•	Sou08
5633.946	4.99	−0.270		•			Sou08
5635.822	4.26	−1.890	•				Sou08
5636.695	3.64	−2.610	•		•		Sou08
5638.262	4.22	−0.870	•	•			Sou08
5641.434	4.26	−1.180	•	•			Sou08
5649.987	5.10	−0.920	•			•	Sou08
5651.468	4.47	−2.000	•				Sou08
5652.317	4.26	−1.950	•				Sou08
5653.864	4.39	−1.640	•			•	Sou08
5655.176	5.06	−0.640	•			•	Sou08
5661.344	4.28	−1.736	•			•	Sou08
5662.516	4.18	−0.573	•	•		•	Sou08
5679.023	4.65	−0.920	•	•	•	•	Sou08
5691.496	4.30	−1.520		•			Sou08
5696.088	4.55	−1.720	•				Sou08
5701.543	2.56	−2.216	•	•			Sou08
5705.464	4.30	−1.355	•				Sou08
5717.832	4.28	−1.130	•	•	•	•	Sou08
5720.886	4.55	−1.950	•		•	•	Sou08

Table A4 – *continued*

λ_{air} [Å]	χ_1 [eV]	$\log gf$	Line list ^a				Reference ^b
			MRD	MPD	MRG	MPG	
5731.761	4.26	−1.300	•	•		•	Sou08
5732.296	4.99	−1.560	•				Sou08
5741.847	4.26	−1.854	•				Sou08
5759.262	4.65	−2.070			•		Sou08
5778.453	2.59	−3.430			•		Sou08
5784.658	3.40	−2.532			•		Sou08
5844.918	4.15	−2.940			•		Sou08
5849.683	3.69	−2.990				•	Sou08
5852.218	4.55	−1.330	•		•		Sou08
5853.148	1.48	−5.280			•	•	Sou08
5855.075	4.61	−1.478	•		•		Sou08
5856.088	4.29	−1.328			•		Sou08
5858.778	4.22	−2.260			•		Sou08
5861.108	4.28	−2.450			•	•	Sou08
5883.816	3.96	−1.360	•	•		•	Sou08
5902.472	4.59	−1.810				•	Sou08
5905.671	4.65	−0.730	•	•	•	•	Sou08
5909.972	3.21	−2.587	•		•	•	Sou08
5916.247	2.45	−2.994	•		•	•	Sou08
5927.788	4.65	−1.090	•		•		Sou08
5929.676	4.55	−1.462	•		•		Sou08
5930.180	4.65	−0.230	•	•	•		Sou08
5934.654	3.93	−1.170	•	•		•	Sou08
5940.991	4.18	−2.150				•	Sou08
5952.718	3.98	−1.440				•	Sou08
5956.693	0.86	−4.605	•	•	•	•	Sou08
6003.011	3.88	−1.120	•	•	•	•	Sou08
6012.209	2.22	−4.038				•	Sou08
6019.365	3.57	−3.360				•	Sou08
6024.057	4.55	−0.120	•	•		•	Sou08
6027.051	4.08	−1.089	•	•	•	•	Sou08
6056.004	4.73	−0.460		•			Sou08
6065.481	2.61	−1.530		•	•		Sou08
6079.007	4.65	−0.729	•	•	•	•	Sou08
6082.710	2.22	−3.573	•		•	•	Sou08
6093.642	4.61	−1.500	•		•	•	Sou08
6094.372	4.65	−1.940				•	Sou08
6096.664	3.98	−1.930	•			•	Sou08
6098.243	4.56	−1.880	•		•	•	Sou08
6120.246	0.91	−5.950			•	•	Sou08
6127.906	4.14	−1.399	•	•		•	Sou08
6136.614	2.45	−1.400		•			Sou08
6136.993	2.20	−2.950		•			Sou08
6137.691	2.59	−1.403		•			Sou08
6151.617	2.18	−3.299	•	•		•	Sou08
6165.359	4.14	−1.474	•	•		•	Sou08
6170.506	4.80	−0.440	•	•			Sou08
6173.334	2.22	−2.880	•	•	•	•	Sou08
6180.202	2.73	−2.586	•				Sou08
6187.989	3.94	−1.720	•		•	•	Sou08
6191.557	2.43	−1.417		•			Sou08
6199.506	2.56	−4.430				•	Sou08
6200.312	2.61	−2.437	•	•		•	Sou08
6213.429	2.22	−2.482	•	•		•	Sou08
6219.280	2.20	−2.433	•	•		•	Sou08
6220.779	3.88	−2.460				•	Sou08
6226.734	3.88	−2.220	•				Sou08
6229.225	2.85	−2.805	•		•	•	Sou08
6230.722	2.56	−1.281	•	•			Sou08
6240.646	2.22	−3.233	•	•	•	•	Sou08
6246.318	3.60	−0.733	•	•	•		Sou08
6252.555	2.40	−1.687	•	•	•	•	Sou08
6265.132	2.18	−2.550	•	•	•	•	Sou08

Table A4 – continued

λ_{air} [Å]	χ_1 [eV]	$\log gf$	Line list ^a				Reference ^b
			MRD	MPD	MRG	MPG	
6270.223	2.86	−2.464	•		•	•	Sou08
6271.278	3.33	−2.703			•	•	Sou08
6280.617	0.86	−4.387		•			Sou08
6290.543	2.59	−4.330				•	Sou08
6297.792	2.22	−2.740		•		•	Sou08
6301.499	3.65	−0.718			•	•	Sou08
6311.499	2.83	−3.141	•			•	Sou08
6315.811	4.08	−1.710	•			•	Sou08
6322.685	2.59	−2.426	•	•	•	•	Sou08
6335.329	2.20	−2.177	•	•	•	•	Sou08
6336.823	3.69	−0.856	•	•	•	•	Sou08
6338.875	4.80	−1.060	•				Sou08
6344.147	2.43	−2.923		•			Sou08
6355.028	2.85	−2.350		•			Sou08
6380.743	4.19	−1.376	•			•	Sou08
6393.600	2.43	−1.432		•	•		Sou08
6400.316	0.91	−4.318	•	•			Sou08
6411.648	3.65	−0.595		•			Sou08
6421.350	2.28	−2.027	•	•			Sou08
6430.845	2.18	−2.006	•	•			Sou08
6469.192	4.83	−0.770	•	•			Sou08
6475.623	2.56	−2.942	•	•			Sou08
6481.869	2.28	−2.984	•	•		•	Sou08
6494.980	2.40	−1.273		•			Sou08
6495.741	4.83	−0.940	•				Sou08
6496.465	4.80	−0.570	•	•		•	Sou08
6498.938	0.96	−4.699	•			•	Sou08
6518.365	2.83	−2.460				•	Sou08
6533.928	4.56	−1.460	•	•	•	•	Sou08
6546.237	2.76	−1.536		•	•	•	Sou08
6574.226	0.99	−5.023	•				Sou08
6581.209	1.48	−4.679				•	Sou08
6591.312	4.59	−2.070			•	•	Sou08
6592.912	2.73	−1.473	•	•		•	Sou08
6593.869	2.43	−2.422	•	•		•	Sou08
6597.561	4.80	−1.070				•	Sou08
6608.025	2.28	−4.030	•			•	Sou08
6609.109	2.56	−2.692	•	•		•	Sou08
6627.543	4.55	−1.680	•				Sou08
6633.412	4.83	−1.490	•				Sou08
6633.748	4.56	−0.799	•				Sou08
6648.079	1.01	−5.429				•	Sou08
6703.565	2.76	−3.160	•		•		Sou08
6710.318	1.48	−4.880	•				Sou08
6713.742	4.80	−1.600	•		•		Sou08
6716.236	4.58	−1.920	•				Sou08
6725.355	4.10	−2.300			•	•	Sou08
6750.151	2.42	−2.621	•	•	•	•	Sou08
6752.707	4.64	−1.204	•	•			Sou08
6783.703	2.59	−3.980	•	•	•		This work
6786.858	4.19	−2.070	•	•	•	•	This work
6793.258	4.08	−2.326	•	•	•		This work
6793.619	4.80	−1.329	•	•	•		This work
6796.123	4.14	−2.530	•		•		This work
6801.865	1.61	−4.829				•	This work
6803.999	4.65	−1.496	•	•			This work
6804.270	4.58	−1.813	•	•			This work
6806.842	2.73	−3.210	•	•	•	•	This work
6810.262	4.61	−0.986	•	•	•	•	This work
6819.588	4.10	−2.764	•		•		This work
6820.371	4.64	−1.320	•	•	•	•	This work
6828.591	4.64	−0.920	•	•	•	•	This work
6833.225	4.64	−2.080	•		•		This work

Table A4 – *continued*

λ_{air} [Å]	χ_1 [eV]	$\log gf$	Line list ^a				Reference ^b
			MRD	MPD	MRG	MPG	
6837.005	4.59	−1.687	•	•	•	•	This work
6838.827	5.84	−0.361	•	•	•		This work
6839.829	2.56	−3.450	•	•	•	•	This work
6841.338	4.61	−0.750	•	•	•		This work
6842.685	4.64	−1.320	•	•	•	•	This work
6843.655	4.55	−0.930	•	•	•	•	This work
6850.435	5.46	−1.053	•		•		This work
6851.635	1.61	−5.320				•	This work
6854.823	4.59	−1.926	•	•			This work
6855.161	4.56	−0.742	•	•	•		This work
6855.712	4.61	−1.820	•	•	•		This work
6857.249	4.08	−2.150	•	•	•	•	This work
6858.148	4.61	−0.930	•	•	•		This work
6859.479	2.85	−4.520				•	This work
6861.937	2.42	−3.890		•			This work
6862.480	4.56	−1.570		•		•	This work
6864.311	4.56	−2.320				•	This work
6885.754	4.65	−1.380		•		•	This work
6911.511	2.42	−4.040				•	This work
6916.680	4.15	−1.450				•	This work
6933.617	2.43	−3.580		•			This work
6945.204	2.42	−2.482				•	This work
6947.488	4.58	−1.611		•			This work
6951.245	4.56	−0.908		•			This work
6971.932	3.02	−3.340	•	•	•	•	This work
6975.426	5.83	−0.215	•	•			This work
6977.428	4.59	−1.564		•		•	This work
6978.850	2.48	−2.500	•	•	•		This work
6988.523	2.40	−3.660		•		•	This work
6999.883	4.10	−1.560	•	•	•		This work
7000.614	4.14	−2.386	•		•	•	This work
7007.965	4.18	−2.060	•	•	•		This work
7011.343	4.59	−1.316		•	•	•	This work
7014.986	2.45	−4.250				•	This work
7016.055	2.42	−3.210		•			This work
7022.390	4.30	−2.290	•		•	•	This work
7022.952	4.19	−1.250		•		•	This work
7024.050	4.08	−2.208	•	•	•		This work
7024.641	4.56	−1.080		•			This work
7038.220	4.22	−1.300	•	•	•		This work
7038.769	4.26	−1.990	•	•	•		This work
7057.953	3.65	−3.380				•	This work
7069.531	2.56	−4.340				•	This work
7071.860	4.61	−1.700				•	This work
7072.791	5.90	−0.882	•				This work
7072.818	4.08	−2.840			•		This work
7083.394	4.91	−1.202	•	•	•	•	This work
7086.724	3.60	−2.356	•	•	•	•	This work
7090.383	4.23	−1.210	•	•	•		This work
7091.921	4.96	−1.298	•		•	•	This work
7095.407	4.21	−2.020	•	•	•		This work
7100.193	2.73	−3.897				•	This work
7107.459	4.19	−1.343		•			This work
7112.167	2.99	−2.998	•	•	•	•	This work
7114.548	2.69	−4.010	•	•	•	•	This work
7118.096	5.01	−1.570	•		•	•	This work
7120.021	4.56	−1.936	•				This work
7127.567	4.99	−1.046	•	•	•		This work
7130.921	4.22	−0.790	•	•	•		This work
7132.986	4.08	−1.628	•		•	•	This work
7142.517	4.96	−0.848		•		•	This work
7145.306	4.61	−1.145	•	•			This work
7151.469	2.48	−3.730	•	•	•	•	This work

Table A4 – continued

λ_{air} [Å]	χ_1 [eV]	$\log gf$	Line list ^a				Reference ^b
			MRD	MPD	MRG	MPG	
7155.630	5.01	−0.725		•			This work
7162.343	5.02	−1.064				•	This work
7179.994	1.48	−4.780	•		•		This work
7212.435	4.96	−0.825	•		•		This work
7219.682	4.08	−1.690	•	•	•	•	This work
7221.202	4.56	−1.184	•	•	•		This work
7223.657	3.02	−2.225				•	This work
7228.695	2.76	−3.380	•	•	•		This work
7239.866	4.21	−1.852				•	This work
7256.134	4.96	−1.590				•	This work
7284.834	4.14	−1.750	•		•	•	This work
7285.275	4.61	−1.700	•		•		This work
7288.736	4.22	−1.035		•			This work
7306.562	4.18	−1.740	•		•	•	This work
7311.074	4.28	−0.967			•		This work
7376.480	6.00	+0.089	•	•	•		This work
7381.333	5.35	−1.087	•		•		This work
7386.333	4.91	−0.267	•		•		This work
7396.507	4.99	−1.640			•		This work
7401.683	4.19	−1.599				•	This work
7411.153	4.28	−0.299	•	•	•	•	This work
7418.666	4.14	−1.376	•	•	•	•	This work
7421.559	4.64	−1.800	•	•	•		This work
7430.538	2.59	−3.860		•			This work
7430.855	4.61	−1.539		•			This work
7435.591	5.31	−0.716	•	•	•	•	This work
7440.911	4.91	−0.573		•	•		This work
7443.022	4.19	−1.820		•		•	This work
7445.748	4.26	−0.102		•			This work
7447.393	4.96	−0.846	•	•	•	•	This work
7453.997	4.19	−2.410	•			•	This work
7461.519	2.56	−3.580	•	•	•	•	This work
7463.382	5.06	−1.720	•		•		This work
7464.293	5.41	−1.066	•		•		This work
7472.750	5.35	−0.994	•				This work
7473.554	4.61	−1.870	•		•		This work
7477.506	3.88	−3.045				•	This work
7484.297	5.09	−1.700	•				This work
7491.647	4.30	−0.900	•	•	•		This work
7495.065	4.22	+0.052		•			This work
7498.530	4.14	−2.250	•	•	•	•	This work
7504.270	5.39	−1.006	•		•		This work
7506.013	5.06	−1.219	•				This work
7507.265	4.42	−1.485	•	•	•	•	This work
7511.018	4.18	+0.099	•	•	•	•	This work
7514.198	5.39	−0.874	•		•	•	This work
7531.143	4.37	−0.951				•	This work
7540.429	2.73	−3.850	•		•	•	This work
7547.896	5.10	−1.350	•		•	•	This work
7551.104	5.09	−1.630	•		•		This work
7559.719	5.06	−1.080	•	•	•		This work
7563.010	4.83	−2.047				•	This work
7568.898	4.28	−0.773	•	•	•	•	This work
7573.413	6.58	+0.302	•		•		This work
7582.121	4.96	−1.750	•		•		This work
7583.788	3.02	−1.885	•	•	•	•	This work
7586.017	4.31	−0.470	•		•	•	This work
7588.844	5.10	−1.672	•				This work
7620.513	4.73	−0.664		•			This work
7689.036	5.10	−1.370				•	This work
7710.363	4.22	−1.113		•		•	This work
7719.048	5.03	−1.153	•	•	•	•	This work
7723.207	2.28	−3.617		•		•	This work

Table A4 – *continued*

λ_{air} [Å]	χ_1 [eV]	$\log gf$	Line list ^a				Reference ^b
			MRD	MPD	MRG	MPG	
7733.723	5.06	−1.536	•		•	•	This work
7745.513	5.09	−1.170	•	•	•	•	This work
7746.595	5.06	−1.284	•	•	•	•	This work
7748.269	2.95	−1.751		•	•	•	This work
7751.108	4.99	−0.754	•	•	•	•	This work
7780.556	4.47	+0.030	•	•	•	•	This work
7802.473	5.09	−1.335	•		•	•	This work
7807.908	4.99	−0.542	•	•	•	•	This work
7832.195	4.43	+0.112	•	•	•	•	This work
7844.558	4.83	−1.810	•		•	•	This work
7855.399	5.06	−1.017		•			This work
7869.609	4.37	−1.880		•			This work
7879.756	5.03	−1.650	•		•	•	This work
7912.866	0.86	−4.848		•			This work
7937.139	4.31	+0.228		•		•	This work
7941.087	3.27	−2.286	•	•	•	•	This work
7945.846	4.39	+0.227		•		•	This work
7954.934	2.99	−3.675	•				This work
7959.142	5.03	−1.212	•	•	•		This work
7998.944	4.37	+0.151		•		•	This work
8028.312	4.47	−0.689		•			This work
8046.046	4.42	+0.032		•			This work
8047.617	0.86	−4.787	•	•	•	•	This work
8075.149	0.91	−5.062		•	•	•	This work
8085.171	4.45	−0.121		•		•	This work
8089.353	5.07	−1.147	•				This work
8090.325	4.58	−1.912	•				This work
8096.875	4.08	−1.776		•		•	This work
8198.920	4.43	−0.566		•			This work
8204.936	0.96	−5.058		•			This work
8207.741	4.45	−0.856	•	•	•	•	This work
8220.377	4.32	+0.275				•	This work
8239.127	2.42	−3.180				•	This work
8248.128	4.37	−0.892		•		•	This work
8293.512	3.30	−2.175		•		•	This work
8327.055	2.20	−1.525		•		•	This work
8340.502	5.07	−1.701	•		•		This work
8342.856	4.99	−1.468	•		•		This work
8349.045	0.91	−5.705				•	This work
8358.520	2.99	−3.145	•		•		This work
8360.793	4.47	−1.688				•	This work
8365.631	3.25	−2.047	•		•	•	This work
8387.771	2.18	−1.493		•		•	This work
8404.395	5.79	−0.705	•				This work
8419.271	6.18	−0.231	•				This work
8422.913	4.14	−2.002		•			This work
8424.141	4.96	−1.156	•	•	•		This work
8439.570	4.55	−0.591		•		•	This work
8447.636	0.96	−6.699				•	This work
8453.657	5.54	−1.043	•		•		This work
8468.406	2.22	−2.072		•			This work
8471.743	4.96	−1.019		•		•	This work
8481.980	4.19	−1.999		•		•	This work
8514.071	2.20	−2.229	•	•	•	•	This work
8515.108	3.02	−2.073	•	•	•		This work
8517.305	6.13	−0.259	•				This work
8526.669	4.91	−0.760		•		•	This work
8571.804	5.01	−1.391				•	This work
8582.257	2.99	−2.134	•	•	•	•	This work
8592.951	4.96	−1.086		•		•	This work
8598.828	4.39	−1.089		•		•	This work
8607.080	5.01	−1.557				•	This work
8611.803	2.85	−1.926	•	•	•	•	This work

Table A4 – continued

λ_{air} [Å]	χ_1 [eV]	$\log gf$	Line list ^a				Reference ^b
			MRD	MPD	MRG	MPG	
8613.939	4.99	− 1.246				•	This work
8616.280	4.91	− 0.707		•		•	This work
8621.601	2.95	− 2.321	•	•	•	•	This work
8632.413	4.10	− 2.409				•	This work
8667.366	2.45	− 4.939				•	This work
8674.746	2.83	− 1.800	•	•	•	•	This work
8678.930	2.45	− 5.418				•	This work
8679.632	4.97	− 1.276	•	•	•		This work
8688.623	2.18	− 1.212	•	•	•	•	This work
8698.706	2.99	− 3.442				•	This work
8699.454	4.96	− 0.380		•		•	This work
8710.392	4.91	− 0.532		•	•		This work
8713.187	2.95	− 2.467		•		•	This work
8729.143	3.41	− 2.872		•		•	This work
8747.425	3.02	− 3.174	•	•	•	•	This work
8757.187	2.85	− 2.059	•	•	•	•	This work
8763.966	4.65	− 0.146	•	•	•	•	This work
8784.440	4.96	− 1.593	•	•	•	•	This work
8793.341	4.61	− 0.092		•			This work
8796.484	4.96	− 1.229	•		•	•	This work
8804.624	2.28	− 3.234	•	•	•	•	This work
8824.219	2.20	− 1.540	•	•	•	•	This work
8828.091	4.96	− 2.240				•	This work
8834.016	4.22	− 2.590				•	This work
8838.428	2.86	− 2.050	•	•	•	•	This work
8846.740	5.01	− 0.781	•	•	•	•	This work
8863.587	4.97	− 1.519				•	This work
8866.931	4.55	+0.083	•	•	•	•	This work
8868.430	3.02	− 2.909	•	•	•	•	This work
8876.024	5.02	− 1.052	•	•	•		This work
8878.250	2.99	− 3.383				•	This work
8897.899	4.91	− 1.937				•	This work
8902.924	4.99	− 2.106				•	This work
8920.013	5.06	− 0.415	•	•	•		This work
8922.650	4.99	− 1.698	•		•	•	This work
8929.075	5.09	− 0.893		•		•	This work
8931.776	3.05	− 3.216				•	This work
8943.065	2.83	− 3.346	•	•		•	This work
8945.189	5.03	− 0.220	•		•	•	This work
8946.260	2.85	− 3.509				•	This work
8950.188	4.15	− 2.425				•	This work
8975.401	2.99	− 2.233	•		•		This work
8978.198	3.41	− 3.457				•	This work
8984.886	5.10	− 0.922	•		•	•	This work
8994.628	3.27	− 3.189				•	This work
8999.556	2.83	− 1.321		•		•	This work
9010.592	2.61	− 2.953				•	This work
9013.977	2.28	− 3.839				•	This work
9019.744	5.10	− 0.988				•	This work
9057.971	3.05	− 4.467				•	This work
9079.579	4.65	− 0.809		•			This work
9080.386	4.96	− 1.104		•			This work
9084.184	4.26	− 2.240				•	This work
9089.404	2.95	− 1.675				•	This work
9103.635	4.18	− 1.921				•	This work
9210.024	2.85	− 2.404	•				This work
9214.499	4.91	− 0.743		•			This work
9258.267	4.61	− 0.725	•	•			This work
9259.005	4.91	− 0.749		•			This work
9800.308	5.09	− 0.453		•			This work
9811.504	5.01	− 1.362				•	This work
9820.241	2.42	− 5.073				•	This work
9834.185	4.99	− 1.214	•				This work

Table A4 – *continued*

λ_{air} [Å]	χ_1 [eV]	$\log gf$	Line list ^a				Reference ^b
			MRD	MPD	MRG	MPG	
9847.457	4.58	−2.305				•	This work
9861.734	5.06	−0.142	•				This work
9868.186	5.09	−0.979	•	•		•	This work
9881.522	4.58	−1.711	•			•	This work
9886.081	5.01	−1.953				•	This work
9889.035	5.03	−0.446	•	•	•	•	This work
9913.180	4.99	−1.266	•		•	•	This work
9924.388	3.55	−3.127	•				This work
9944.207	5.01	−1.338	•	•	•	•	This work
9951.157	5.39	−1.267	•	•	•	•	This work
9953.470	5.45	−1.309				•	This work
9970.233	3.02	−4.818				•	This work
9977.641	5.06	−1.660	•		•		This work
9980.463	5.03	−1.379	•		•	•	This work
9999.924	5.50	−1.421				•	This work
10041.472	5.01	−1.772				•	This work
10065.045	4.83	−0.289	•	•	•	•	This work
10081.393	2.42	−4.537				•	And16
10086.242	2.95	−4.054				•	This work
10089.776	5.45	−1.247				•	This work
10114.014	2.76	−3.692	•	•	•	•	This work
10137.100	5.09	−1.708	•		•	•	And16
10142.844	5.06	−1.510	•		•		And16
10145.561	4.80	−0.177	•	•			This work
10155.162	2.18	−4.226	•	•	•	•	And16
10167.468	2.20	−4.117	•	•	•	•	And16
10195.105	2.73	−3.580	•		•	•	And16
10216.313	4.73	−0.063		•		•	This work
10218.408	3.07	−2.760		•		•	This work
10227.994	6.12	−0.354	•		•		And16
10230.795	6.12	−0.339	•		•	•	And16
10252.551	5.83	−1.026				•	This work
10262.471	5.48	−1.613				•	This work
10265.217	2.22	−4.537	•		•	•	And16
10307.454	4.59	−2.067				•	This work
10332.327	3.64	−2.938	•		•	•	And16
10333.184	4.59	−2.585				•	This work
10340.885	2.20	−3.577	•	•	•	•	And16
10347.965	5.39	−0.551	•	•	•	•	And16
10353.804	5.39	−0.819	•	•	•	•	And16
10364.062	5.45	−0.960	•		•	•	And16
10378.999	2.22	−4.148		•			And16
10388.744	5.45	−1.468				•	And16
10395.794	2.18	−3.393	•			•	This work
10423.027	2.69	−3.616		•		•	This work
10423.743	3.07	−2.918	•	•	•	•	And16
10435.355	4.73	−1.945				•	This work
10469.652	3.88	−1.184	•	•		•	This work
10532.234	3.93	−1.480	•	•	•	•	And16
10555.649	5.45	−1.108	•		•	•	And16
10577.139	3.30	−3.136	•	•	•	•	And16
10611.686	6.17	+0.021	•	•	•	•	And16
10616.721	3.27	−3.127	•	•	•	•	And16
10674.070	6.17	−0.466	•		•	•	And16
10742.550	3.64	−3.629				•	This work
10753.004	3.96	−1.845	•	•		•	This work
10754.753	2.83	−4.523				•	This work
10780.694	3.24	−3.289	•		•	•	And16
10783.050	3.11	−2.567	•	•		•	This work
10818.274	3.96	−1.948	•	•	•	•	And16
10849.465	5.54	−1.444				•	This work
10863.518	4.73	−0.895				•	This work
10881.758	2.85	−3.604		•		•	This work

Table A4 – continued

λ_{air} [Å]	χ_1 [eV]	$\log gf$	Line list ^a				Reference ^b
			MRD	MPD	MRG	MPG	
10884.262	3.93	− 1.925	•	•		•	This work
10888.606	2.28	− 5.433				•	This work
10896.299	3.07	− 2.694	•			•	This work
11026.788	3.94	− 2.805				•	And16
11045.599	5.59	− 0.624				•	This work
11071.712	3.07	− 4.281				•	This work
12053.082	4.56	− 1.543	•		•	•	And16
12283.298	6.17	− 0.537	•		•	•	And16
12485.492	2.42	− 5.379				•	This work
12510.519	4.96	− 1.605	•		•	•	And16
12545.946	4.08	− 3.485				•	This work
12556.996	2.28	− 3.626	•		•	•	And16
12615.928	4.64	− 1.517	•		•		And16
12638.703	4.56	− 0.783		•			This work
12648.741	4.61	− 1.140		•			And16
12789.450	5.01	− 1.514				•	This work
12807.152	3.64	− 2.452	•	•	•	•	And16
12808.243	4.99	− 1.362	•		•	•	And16
12824.859	3.02	− 3.835	•		•	•	And16
12879.766	2.28	− 3.458	•			•	This work
12933.006	5.02	− 1.548	•		•	•	And16
12934.666	5.39	− 0.948			•	•	And16
12946.532	3.25	− 4.754				•	This work
13014.841	5.45	− 1.693				•	And16
13098.876	5.01	− 1.290				•	This work
13352.173	5.31	− 0.521	•		•		And16
14939.644	6.47	− 0.153				•	This work
14979.696	6.17	− 0.451				•	And16
14982.801	6.26	− 0.495	•		•		And16
14988.778	6.17	+0.186	•				This work
15013.771	6.22	+0.087				•	This work
15017.700	6.22	+0.062	•	•	•	•	And16
15160.503	6.34	− 0.253	•		•		This work
15176.713	5.92	− 0.497	•		•		And16
15194.490	2.22	− 4.815	•		•	•	And16
15201.562	6.31	− 0.161				•	And16
15207.526	5.39	+0.323	•	•	•	•	And16
15219.618	5.59	− 0.825	•		•	•	And16
15224.729	5.96	− 0.315	•		•	•	And16
15239.712	6.42	− 0.032			•	•	And16
15244.973	5.59	− 0.072				•	This work
15293.135	6.31	+0.143	•				This work
15294.560	5.31	+0.719	•	•		•	This work
15301.557	5.92	− 0.687	•		•	•	This work
15335.383	5.41	+0.088	•				And16
15343.788	5.65	− 0.582	•	•	•	•	This work
15348.966	5.95	− 1.260	•		•		This work
15375.346	5.92	− 0.991	•		•	•	And16
15394.673	5.62	+0.008	•		•	•	And16
15395.718	5.62	− 0.126	•	•	•	•	And16
15514.279	6.29	− 0.473	•				And16
15522.607	6.32	− 1.118	•			•	And16
15524.308	5.79	− 0.881	•		•	•	And16
15531.751	5.64	− 0.243	•	•	•	•	And16
15534.245	5.64	− 0.382	•	•	•	•	And16
15542.079	5.64	− 0.337	•	•	•	•	And16
15550.436	6.32	− 0.102	•		•	•	And16
15551.433	6.35	− 0.371	•		•	•	And16
15560.784	6.35	− 0.475	•		•		And16
15565.222	6.32	− 0.557	•		•		And16
15566.725	6.35	− 0.681			•	•	And16
15588.259	6.37	+0.419	•	•	•		And16
15590.046	6.24	− 0.829	•			•	And16

Table A4 – *continued*

λ_{air} [Å]	χ_1 [eV]	$\log gf$	Line list ^a				Reference ^b
			MRD	MPD	MRG	MPG	
15591.490	6.24	+0.874	•	•	•	•	And16
15593.749	5.03	−1.922	•		•		And16
15598.869	6.24	−0.236			•		And16
15604.220	6.24	+0.538	•	•	•	•	This work
15611.145	3.41	−3.768			•	•	And16
15621.654	5.54	+0.589	•	•		•	This work
15645.016	6.31	−0.390	•		•	•	This work
15648.510	5.43	−0.599	•	•	•	•	And16
15652.871	6.25	−0.161	•	•	•		And16
15662.013	5.83	+0.371	•	•	•	•	And16
15665.240	5.98	−0.337	•	•			This work
15682.513	6.37	−0.265	•		•	•	And16
15691.853	6.25	+0.649	•				And16
15723.586	5.62	−0.143	•	•	•		And16
15731.412	6.45	−0.337			•		And16
15733.509	6.25	−0.978	•				And16
15788.996	6.25	+0.490	•				And16
15920.642	6.26	+0.366	•		•		This work
15928.158	5.95	−0.680	•		•	•	And16
15929.472	6.31	−0.383	•			•	And16
15934.017	6.31	−0.294	•		•	•	And16
15938.918	6.37	+0.065				•	This work
15940.918	5.81	−1.594	•			•	And16
15941.848	6.36	+0.265	•	•	•		And16
15962.558	6.42	−0.078	•		•	•	This work
15964.865	5.92	+0.279	•	•	•	•	And16
15980.725	6.26	+0.958	•	•			And16
16009.610	5.43	−0.470	•	•			And16
16040.654	5.87	+0.317	•		•		And16
16051.734	6.26	−0.942	•		•		And16
16070.180	5.96	−0.569	•		•		And16
16071.397	6.27	+0.102	•				And16
16100.282	6.35	−0.043				•	And16
16102.408	5.87	+0.546	•		•		And16
16125.899	6.35	+0.860		•		•	This work
16156.557	5.96	−0.294	•			•	And16
16165.029	6.32	+0.988	•	•		•	And16
16171.930	6.38	−0.445	•		•	•	And16
16174.975	6.38	+0.185	•	•	•	•	And16
16177.991	6.38	−0.402		•	•	•	And16
16179.583	6.32	+0.261	•	•	•	•	And16
16180.900	6.28	+0.295	•	•	•	•	And16
16182.170	6.32	−0.708			•		This work
16185.799	6.39	+0.264		•			This work
16195.060	6.39	+0.467	•	•	•		And16
16198.502	5.41	−0.444	•	•	•	•	And16
16201.513	6.38	−0.329	•		•		This work
16207.744	6.32	+0.585	•	•	•		And16
16377.388	6.36	−0.465	•		•	•	And16
16384.141	6.36	−0.736			•	•	And16
16394.389	5.96	+0.358	•	•	•	•	And16
16396.306	6.28	−0.530	•				This work
16404.601	6.36	+0.581	•		•		And16
16407.786	6.29	+0.007	•	•			This work
16436.621	5.92	+0.007	•		•		And16
16440.394	6.29	−0.241	•		•		And16
16444.816	5.83	+0.663	•	•	•		And16
16466.921	6.39	+0.003	•	•	•	•	And16
16471.753	6.37	+0.030	•			•	And16
16474.077	6.02	−0.959	•	•		•	And16
16481.228	6.39	−0.162	•				This work
16486.666	5.83	+0.783	•		•	•	This work
16506.293	5.95	−0.463			•		This work

Table A4 – continued

λ_{air} [Å]	χ_I [eV]	$\log gf$	Line list ^a				Reference ^b
			MRD	MPD	MRG	MPG	
16537.994	6.29	−0.867	•				This work
16539.193	6.34	−0.119	•				And16
16544.667	6.34	−0.029	•		•	•	And16
16551.994	6.41	+0.338	•		•	•	And16
16557.148	6.41	−1.083				•	This work
16559.677	6.40	+0.210				•	And16
16561.764	5.98	+0.243		•			And16
16586.051	5.62	−0.753			•	•	And16
16612.761	6.40	+0.286	•		•		And16
16629.836	6.57	−0.435	•				This work
16645.874	5.96	−0.032	•	•	•	•	And16
16807.435	5.83	−1.301			•		And16
16833.052	5.96	−0.889	•		•	•	And16
16843.228	5.87	−1.321	•				And16
16865.513	6.41	−0.749				•	And16
16869.950	6.41	−0.415			•		This work
16874.116	6.35	−0.159	•				And16
16892.384	6.31	−0.799	•		•	•	This work
16969.910	5.95	−0.069			•		This work
17005.450	6.07	+0.005		•		•	This work
17008.971	6.62	−0.301	•		•		This work
17011.095	5.95	+0.102	•			•	This work
17037.787	6.39	−0.852				•	And16

^a**Line lists.** MRD: metal-rich dwarfs; MPD: metal-poor dwarfs; MRG: metal-rich giants; MPG: metal-poor giants.

^b**References.** Sou08: Sousa et al. (2008); And16: Andreasen et al. (2016).

Table A5. Merged Fe II line lists.

λ_{air} [Å]	χ_{II} [eV]	$\log gf$	Line list ^a				Reference ^b
			MRD	MPD	MRG	MPG	
5325.552	3.22	−3.160		•		•	Sou08
5414.070	3.22	−3.580			•		Sou08
5425.248	3.20	−3.220	•	•	•	•	Sou08
5534.838	3.24	−2.730		•			Sou08
5991.371	3.15	−3.540	•				Sou08
6084.102	3.20	−3.780	•		•		Sou08
6149.246	3.89	−2.720	•		•	•	Sou08
6238.386	3.89	−2.754		•	•		Sou08
6247.557	3.89	−2.310		•			Sou08
6369.459	2.89	−4.160	•			•	Sou08
6416.919	3.89	−2.650	•				Sou08
6432.676	2.89	−3.520	•	•	•		Sou08
6456.380	3.90	−2.100		•	•	•	Sou08
6516.077	2.89	−3.320	•	•			Sou08
7222.391	3.89	−3.360	•	•	•		This work
7224.478	3.89	−3.240	•	•	•		This work
7449.329	3.89	−3.090	•		•		This work
7479.693	3.89	−3.680	•		•		This work
7515.830	3.90	−3.460	•		•		This work
7533.368	3.90	−3.600	•		•		This work
7711.720	3.90	−2.500	•	•	•	•	This work
9997.598	5.48	−1.867	•		•		This work
10501.503	5.55	−2.086	•				And16

^a**Line lists.** MRD: metal-rich dwarfs; MPD: metal-poor dwarfs; MRG: metal-rich giants; MPG: metal-poor giants.

^b**References.** Sou08: Sousa et al. (2008); And16: Andreasen et al. (2016).

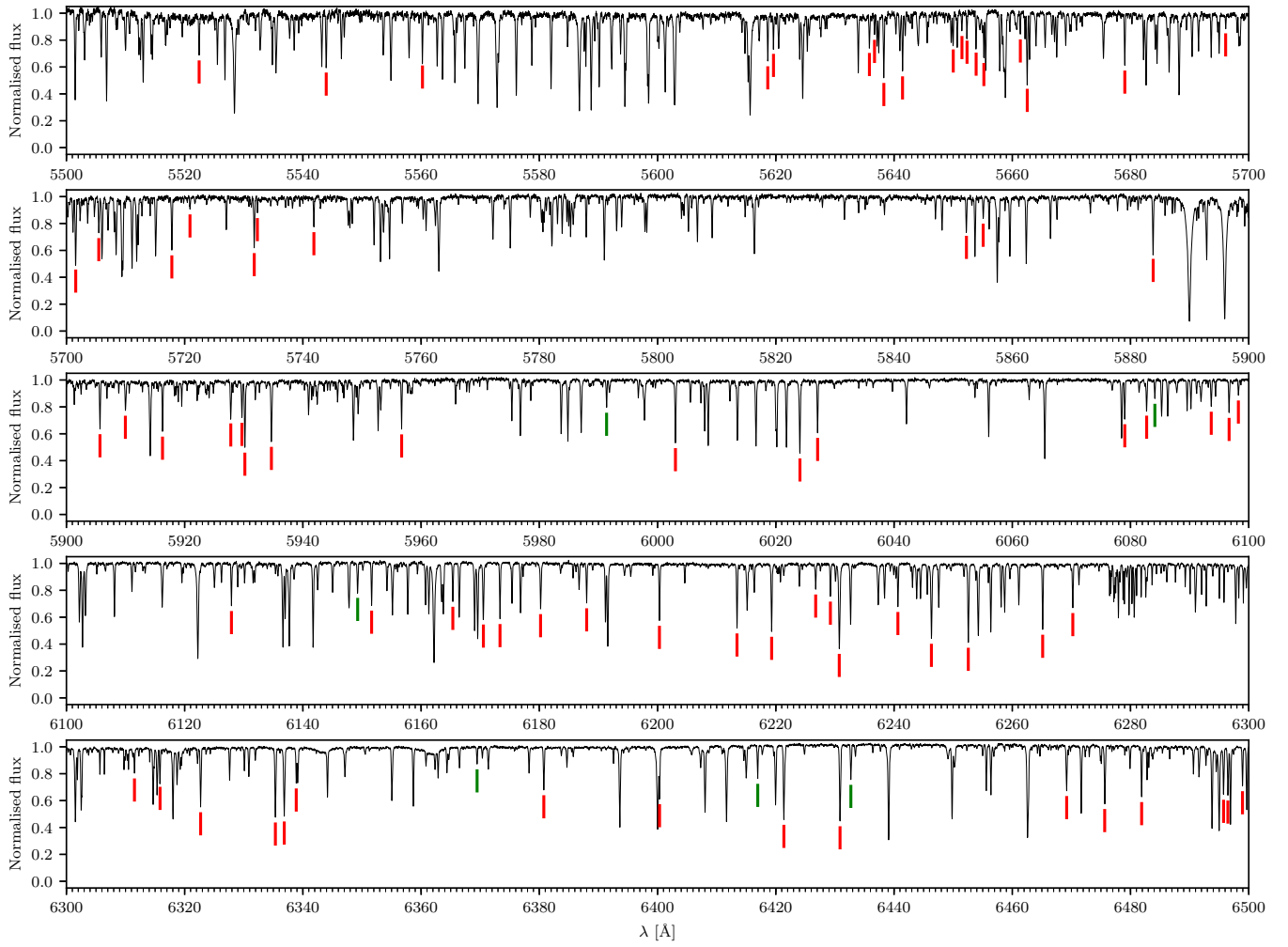
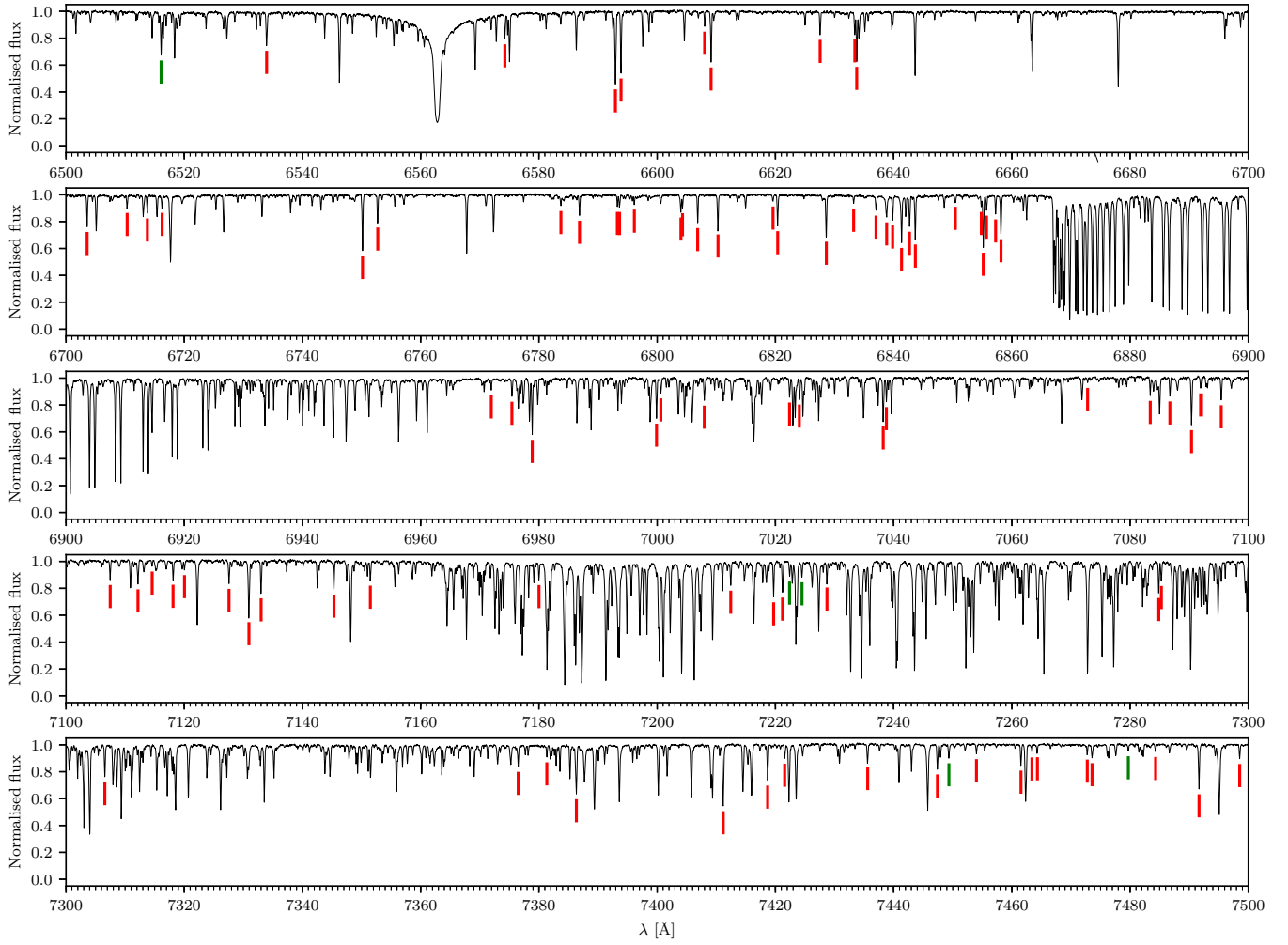
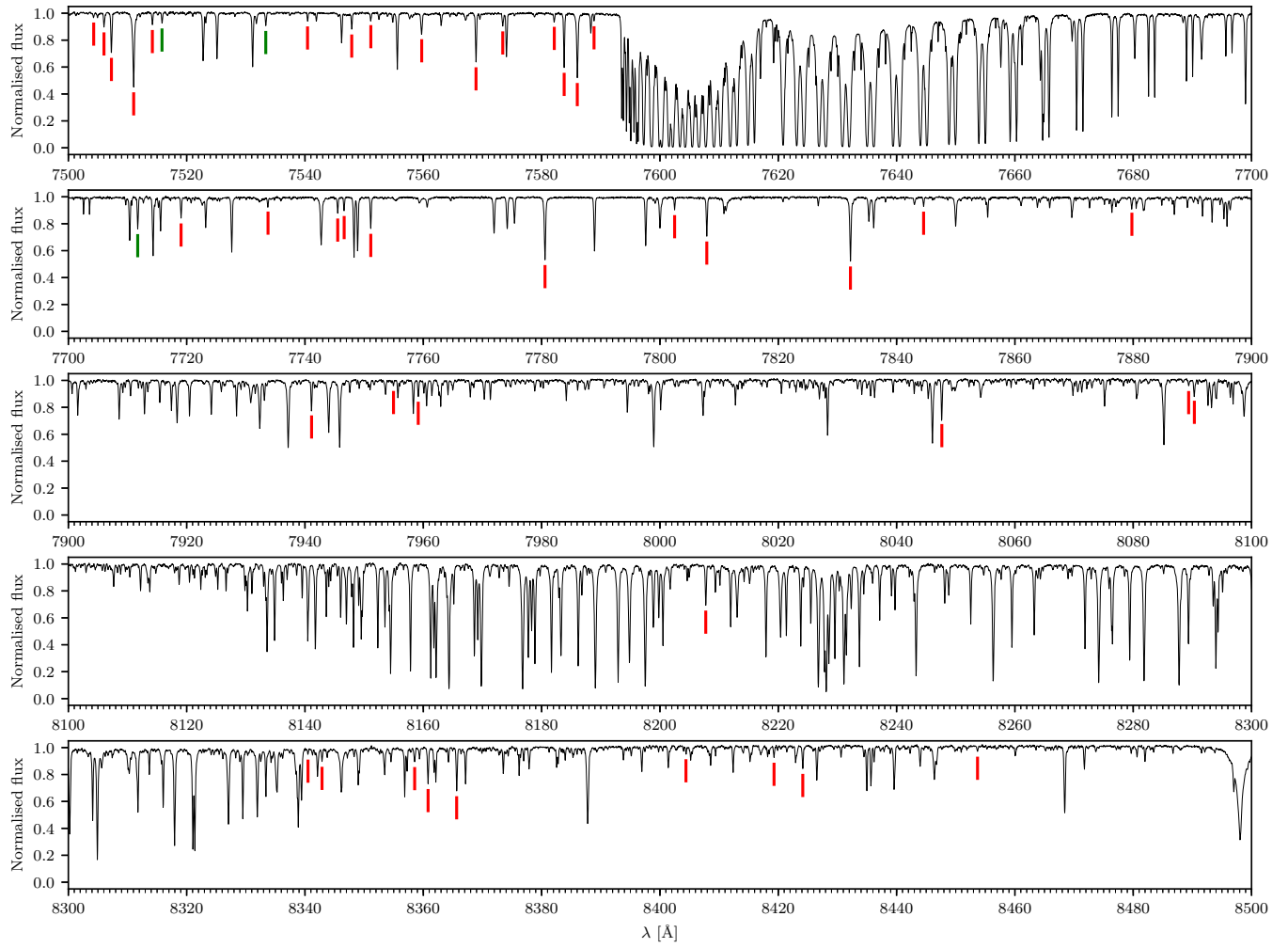
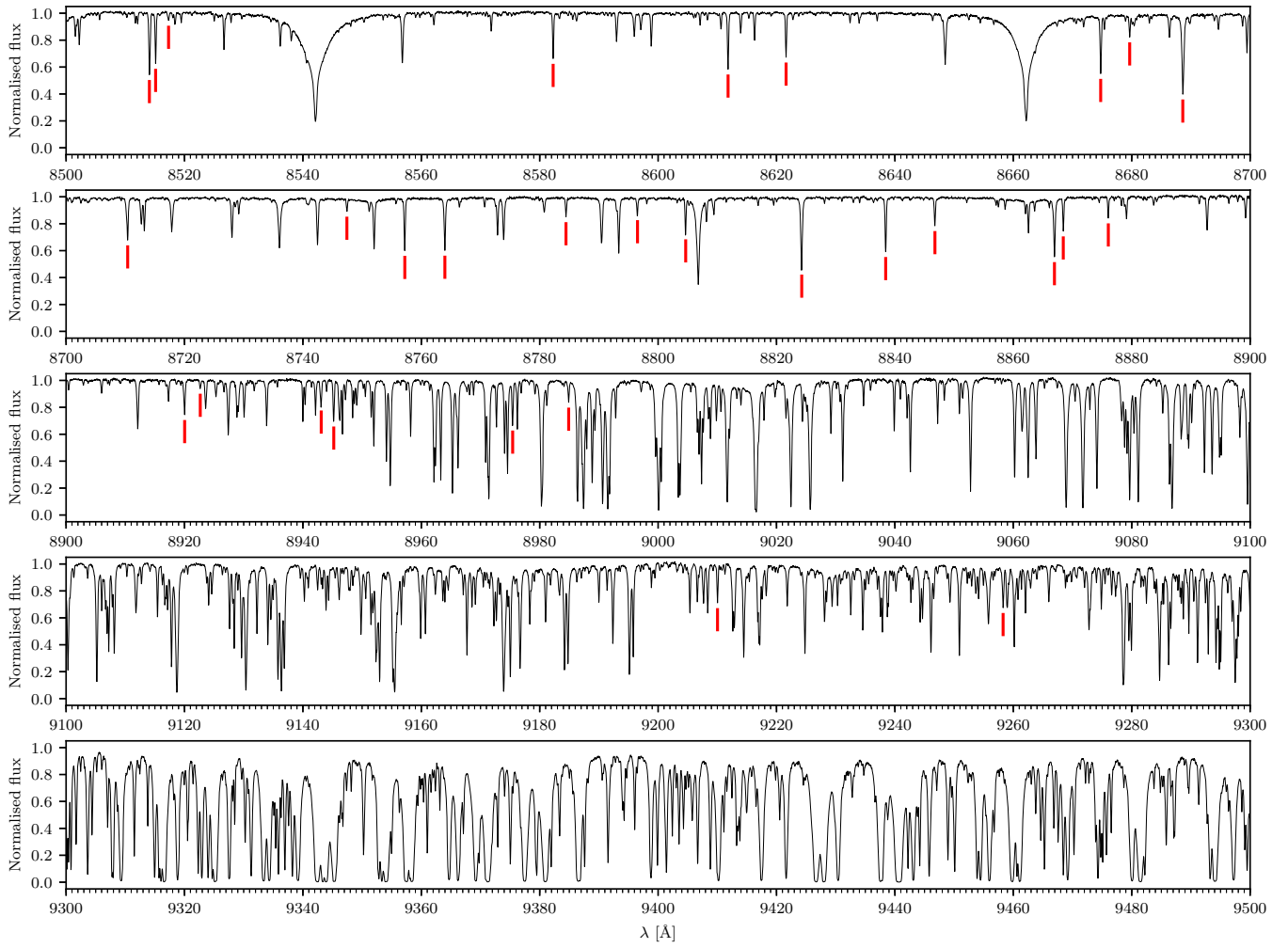
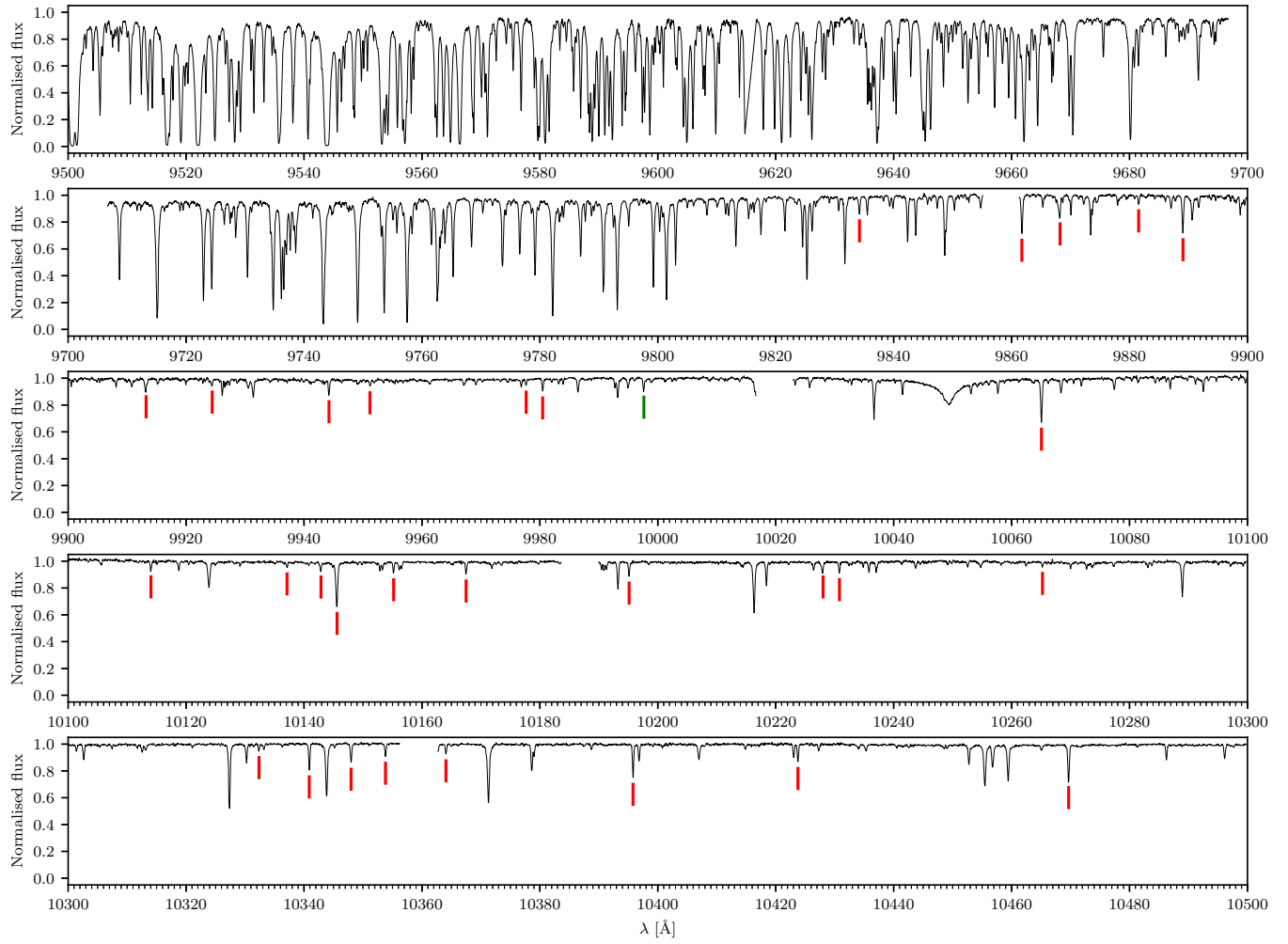


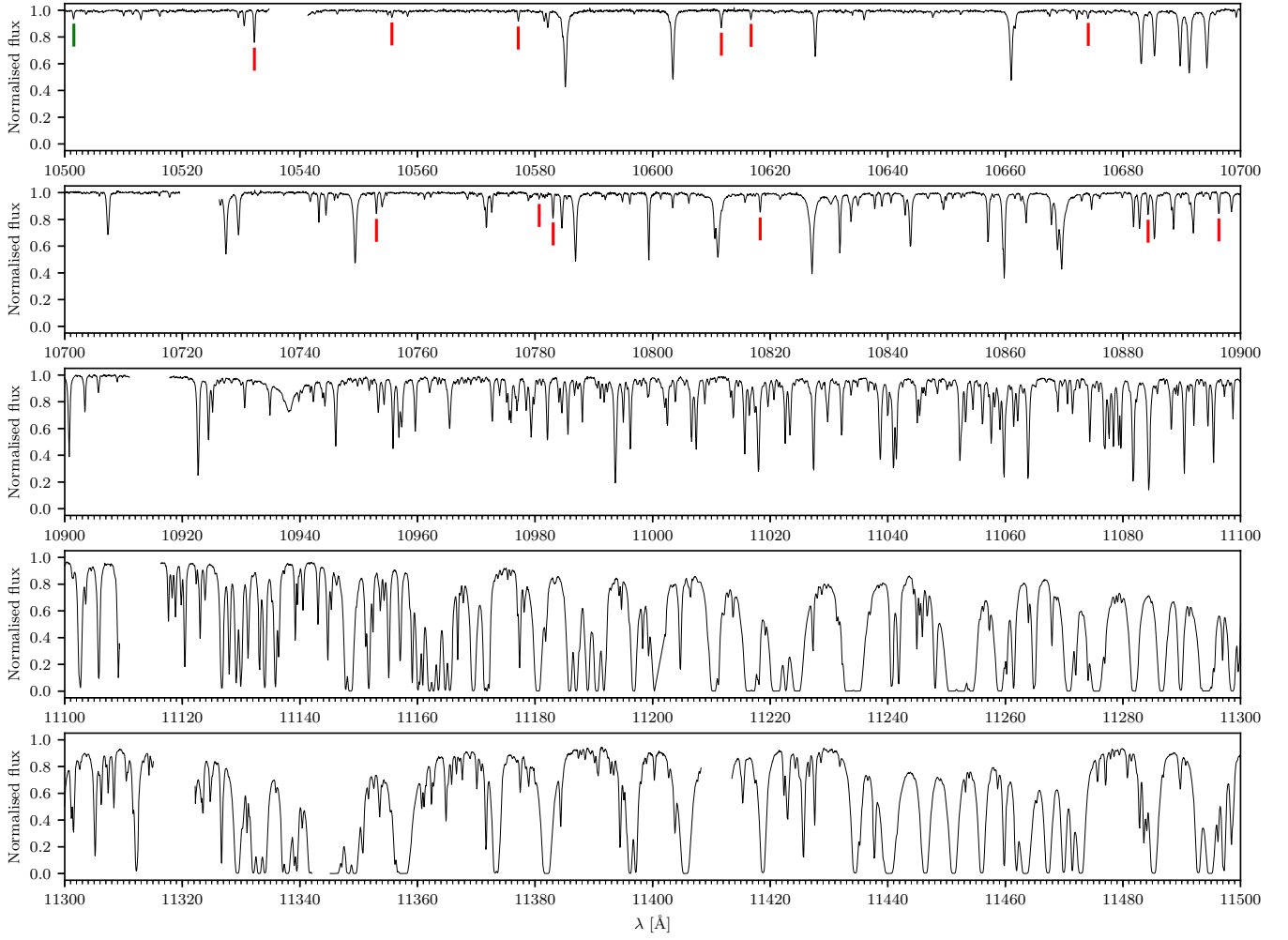
Figure A1. CARMENES spectrum of 18 Sco. Fe I and Fe II lines are shown in red and green, respectively.

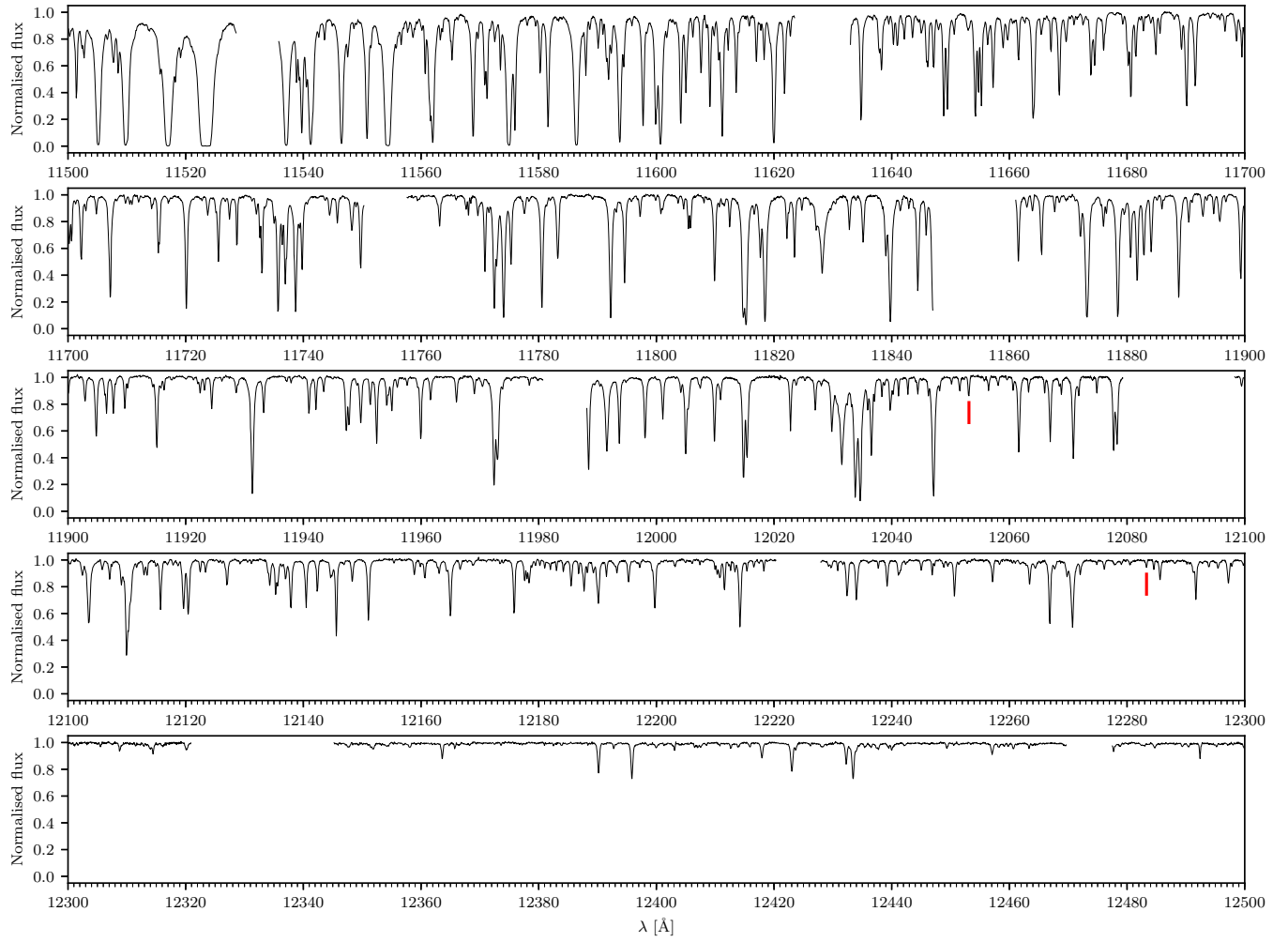
Figure A1. *continued*

Figure A1. *continued*

Figure A1. *continued*

Figure A1. *continued*

Figure A1. *continued*

**Figure A1.** *continued*

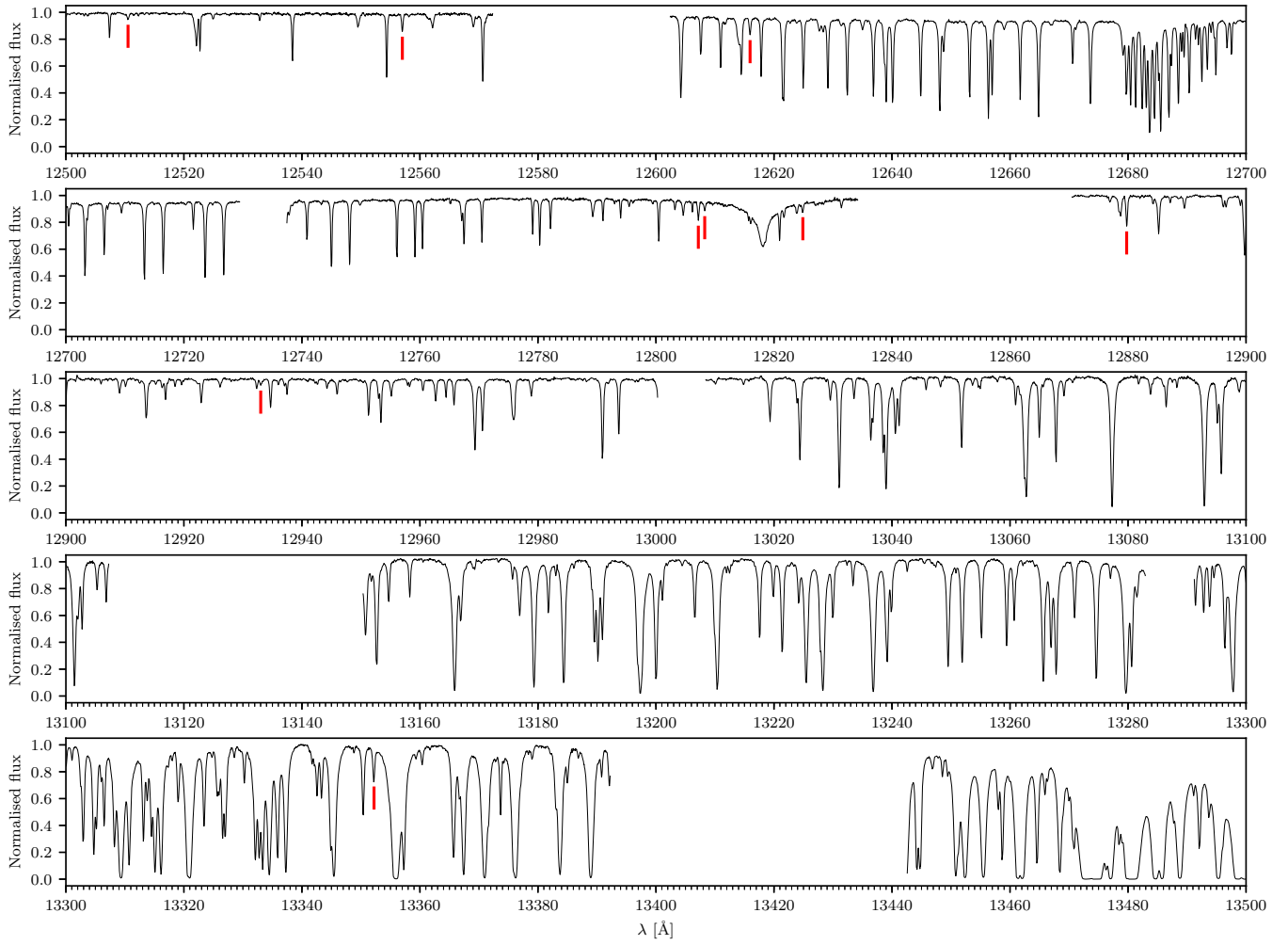
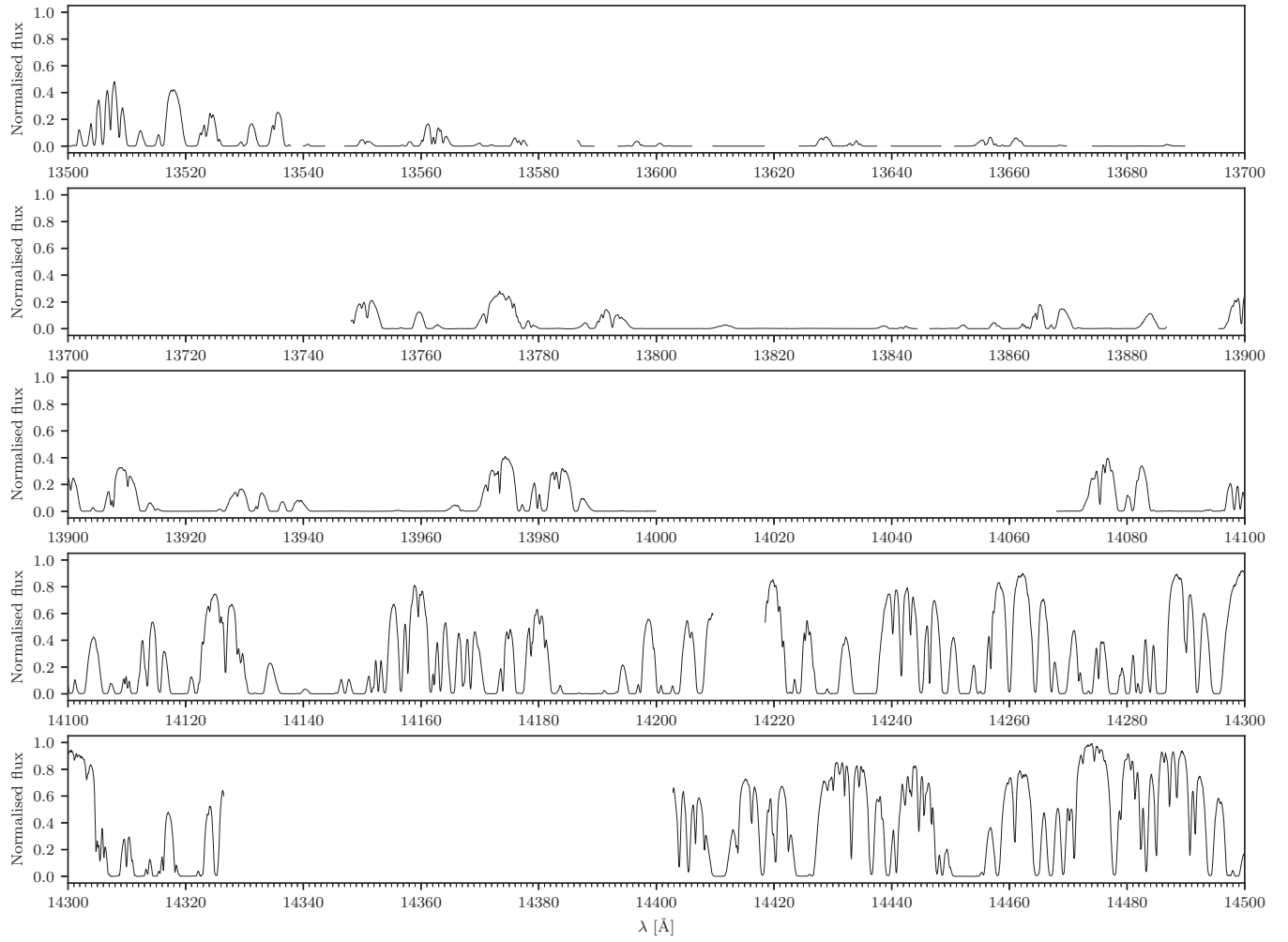


Figure A1. continued

**Figure A1.** *continued*

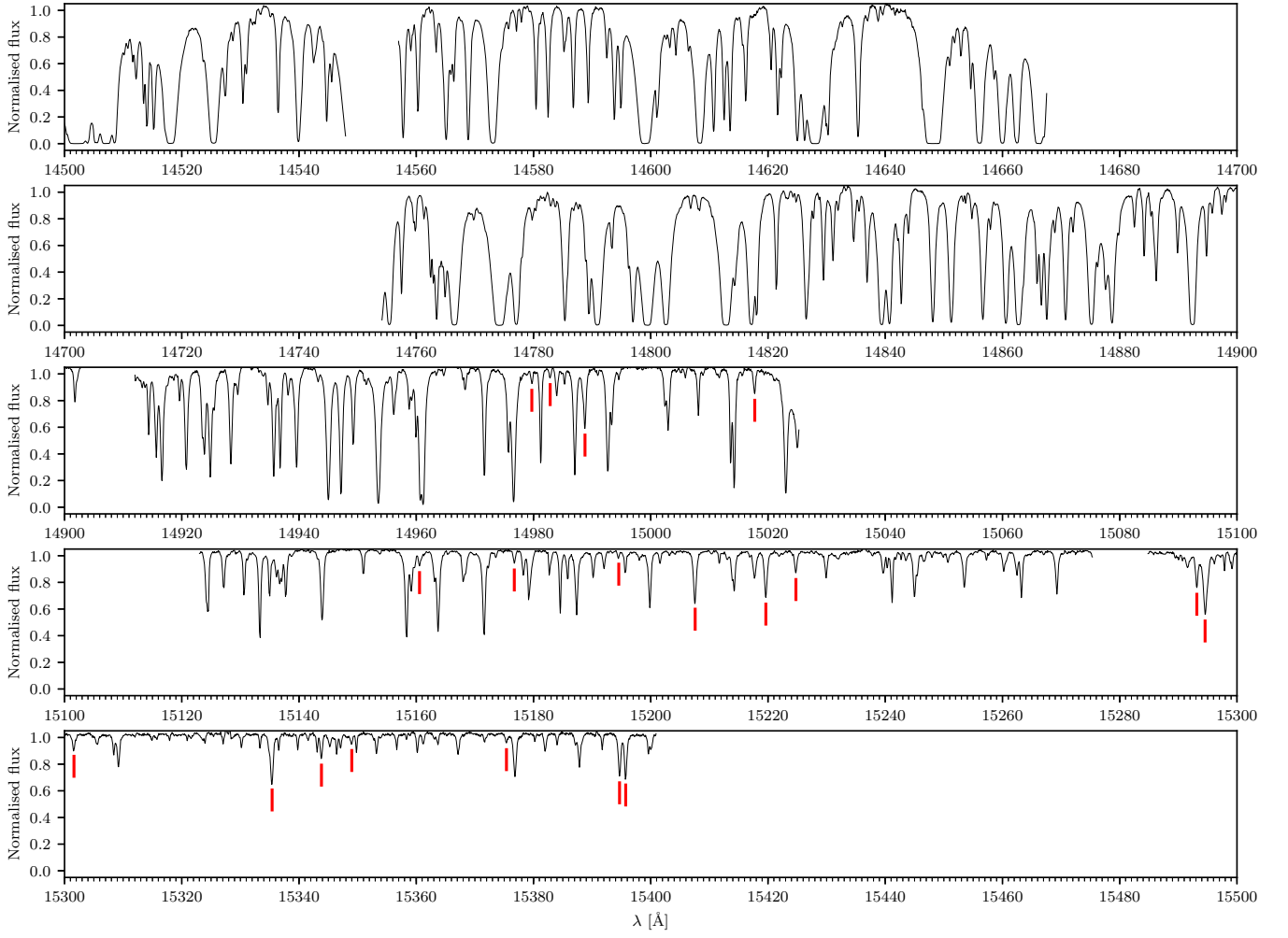
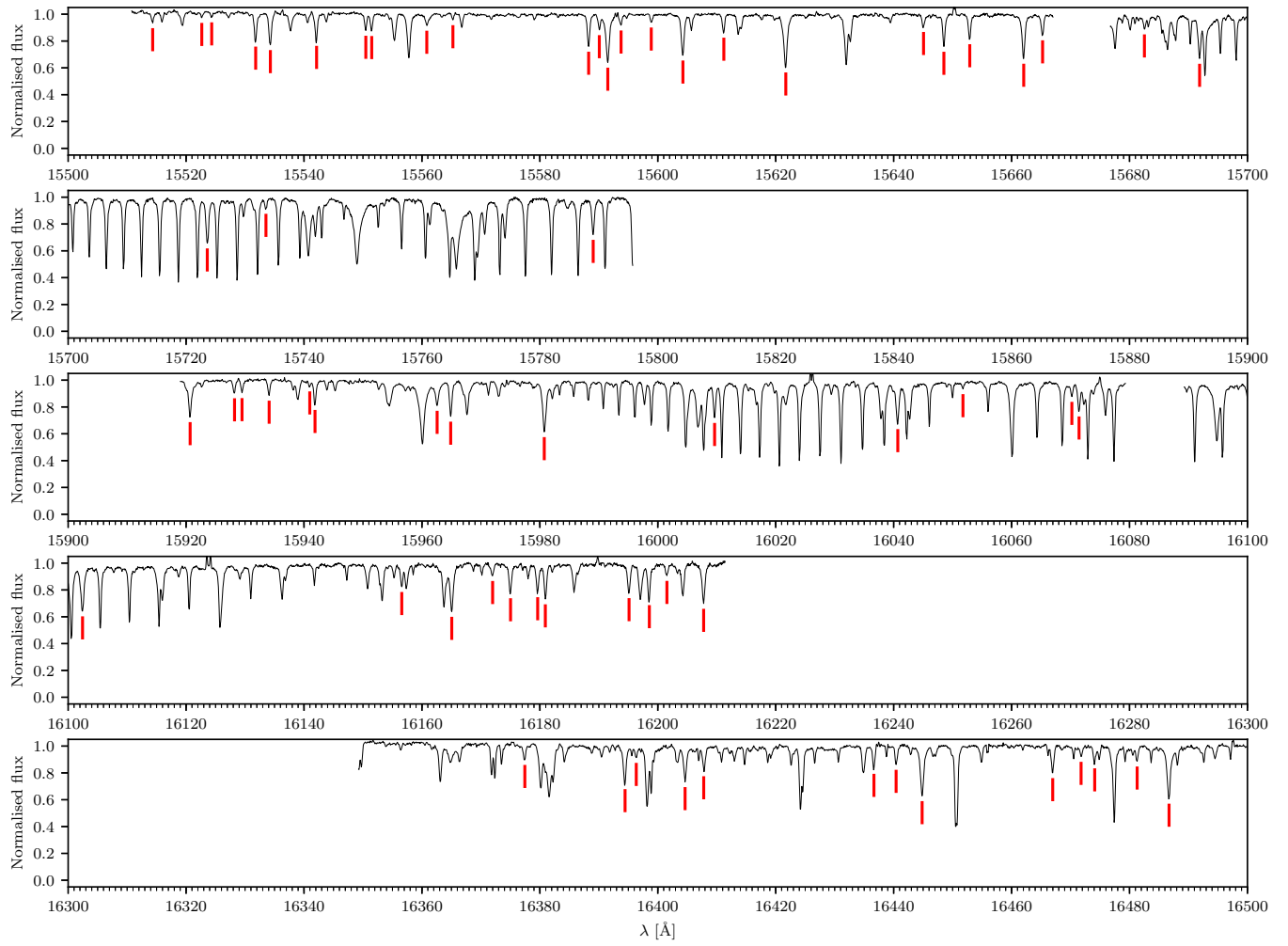
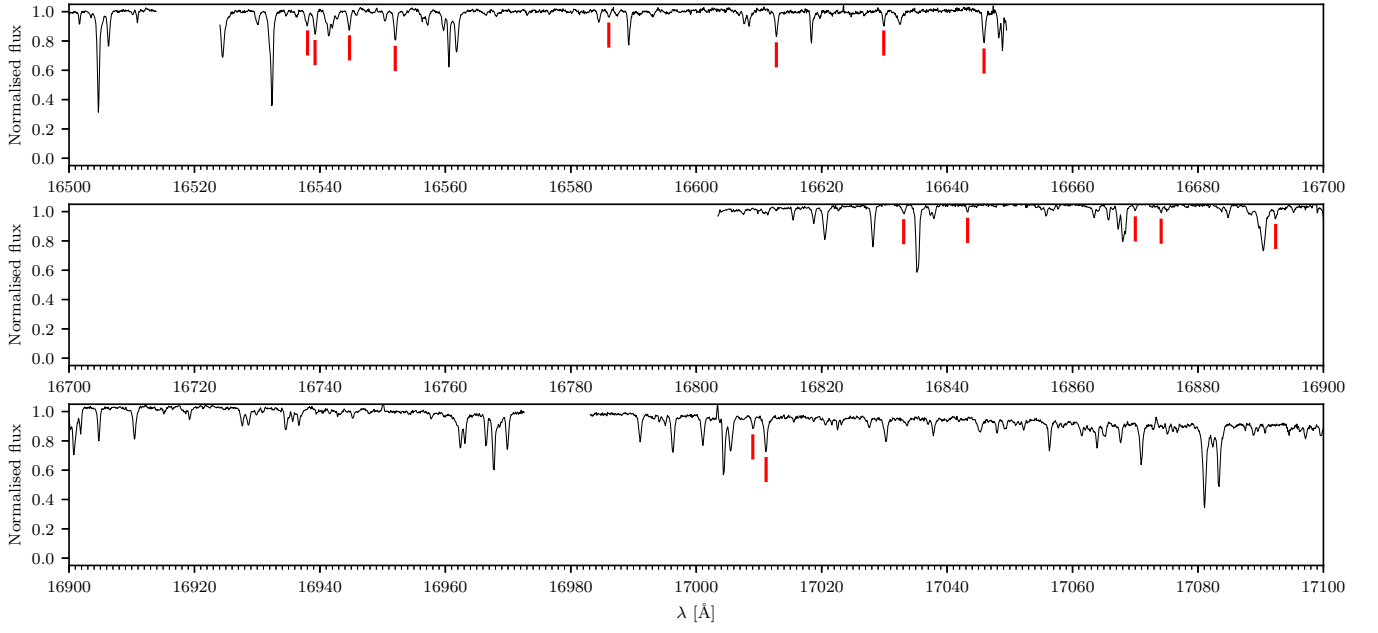


Figure A1. continued

Figure A1. *continued*

Figure A1. *continued*

This paper has been typeset from a \LaTeX file prepared by the author.